Numerical simulation of double-diffusive convection in a rectangular box

Y. Young and R. Rosner
Department of Astronomy and Astrophysics, The University of Chicago, 5640 South Ellis Avenue, Chicago, Illinois 60637
(Received 13 October 1998)

We directly simulate incompressible, double-diffusive convection in a vertical slot using a two-dimensional pseudospectral code. Incompressibility is achieved in our code by the consistent implementation of the tau correction. We find that layer dynamics depends on the particulars of the imposed boundary conditions for the temperature at the sidewalls and the density stratification ratio (the relative strength of the stabilizing solute gradient to the destabilizing horizontal thermal difference). We demonstrate the effects of the density stratification ratio on the layer dynamics by adopting three stratification ratios for the constant sidewall temperature case. We perform one simulation for constant lateral heat flux to study the effects of the temperature boundary conditions. We apply the argument for layering in turbulent stratified fluids to our problem, and find—despite the tilted nature of cell boundaries in our case—similarities in both the averaged equations and actual layer evolution. Finally, we provide details for both edge mergers and interior mergers.

PACS number(s): 47.17.+e, 47.20.Ky, 47.27.−i

I. INTRODUCTION

Double-diffusive convection, in which two diffusive species (with different diffusivities) compete to determine the convective stability of a fluid, is ubiquitous in both terrestrial and astrophysical environments [1]. Of special interest are cases where the total density is stably stratified, while the less diffusive species (''solute'') is stabilizing and the more diffusive species (''temperature'') is destabilizing; this is sometimes referred to as the diffusive regime [1]. In this paper we study this phenomenon in the context of vertical ''slot convection,'' e.g., in the case for which the destabilizing heat flux is horizontal (perpendicular to gravity) and defined either by a constant lateral heat flux at the sidewall or by a constant temperature difference across the slot.

Double-diffusive slot convection has different regimes of stabilities as the relative strength of stabilizing solute to the destabilizing temperature varies. Such systems were studied by Turner and Stommel [2] and Turner [3]; and Thorpe, Hutt, and Soulsby [4] demonstrated that a simplified two-dimensional model suffices to explain the experiments (for large solute Rayleigh numbers). Since then, double-diffusive slot convection has been extensively studied both experimentally and theoretically [5–11], including complete linear and weakly nonlinear analyses of the steady initial state in an infinitely long vertical slot [12,13]. Kerr [14,15] has studied cases for which the sidewall temperatures are turned on instantaneously (impulsive heating) and finds good agreement with comparable results for the steady initial background states. Numerical studies of double-diffusive slot convection were carried out by Wirtz, Briggs, and Chen [16]; these and subsequent studies by Wirtz [17], Heinrich [18], and Lee and Hyun [19] are able to reproduce general results, such as layer depth and the critical solute Rayleigh numbers, but did not consider the details of the layer dynamics, such as the merging or decay of layers. More recently, Wright and Shyy [20] used a composite grid method to simulate double-diffusive convection in a square box heated laterally at a constant rate. Their results identify three regimes of layer formation and interaction as the sidewall heat flux is varied, but their analysis was primarily qualitative. In this study we use a two-dimensional Chebyshev pseudospectral code to simulate incompressible, double-diffusive slot convection, focusing on a quantitative investigation of layer evolution.

The incompressible Navier-Stokes equations are solved using the influence matrix technique [21] with Tuckerman's algorithm for tau correction [22]. Others have used similar algorithms without the complete multidimensional tau correction ([23] and references therein), arguing that the resulting errors (viz., nonvanishing flow divergence) are balanced by the inefficiency of the tau correction, and that these errors become ignorable as the number of grid points is increased. We discuss this point in detail in Sec. II B below.

Layer formation is also known to occur in stratified turbulent fluids, in which an initially stably stratified fluid is stirred by a horizontally moving grid or rod [24,25], and it has been shown that the horizontally averaged buoyancy gradient plays a central role in such layering [26]. Balmforth, Smith, and Young [27] reproduce such layer dynamics by solving two equations coupling both the buoyancy gradient and the kinetic energy density to some external forcing. In our cases, where solute Rayleigh numbers are large, layers are weakly driven compared to those in turbulently driven stratified fluid, but we adopt the methodology in [26,27] to describe the weakly driven layer dynamics: we quantitatively describe the layer dynamics by investigating the dynamics of the horizontally averaged quantities, such as the buoyancy gradient, buoyancy flux, kinetic energy density, horizontal stratification, and the two Nusselt numbers. Results show that the mean quantities describe the layer dynamics well, even though the horizontal average is taken across the tilting layer boundaries in our cases; and we find similar layer dynamics to those described in [27].

This paper is organized as follows: in the next section we discuss the numerics. In Sec. III we summarize the various parameters characterizing the layer formation found in the previous literature. In Sec. IV we present our results, considering the cases of both fixed sidewall temperature and constant lateral heat flux. We discuss layer merging and summarize our results in Sec. V.

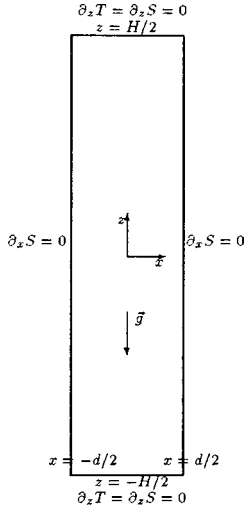

FIG. 1. Sketch of the vertical slot of width d and height H, filled with incompressible fluid. No-slip boundary conditions for the velocity and no-flux boundary conditions for the solute are adopted. We also adopt insulating boundary conditions for the temperature at top and bottom end wall. The initial state is a static state with a stably stratified solute gradient. The sidewall temperatures are impulsively turned on at the beginning of the simulation.

II. EQUATIONS AND NUMERICAL ALGORITHMS

A. Equations

We consider a two-dimensional (2D) rectangular box of width d and height H (Fig. 1), which we assume to be filled by an incompressible fluid ($\vec{\nabla}\cdot\vec{u}=0$) coupled to two scalar fields through the buoyancy effect [1,28]. The two scalar fields (in our case, temperature and solute) have different diffusivities; their evolution is described by advective diffusion equations, with temperature (T) being more diffusive than solute (S) (i.e., the thermal diffusivity κ_t is greater than the solute diffusivity κ_s). The governing equations are nondimensionalized by scaling the length by $d/2$, time by $(d/2)^2/\kappa_t$ (the thermal diffusion time), velocity by $\kappa_t/(d/2)$, temperature by $(\Delta T)/2$ if the temperature is fixed at the sidewalls (or by $|\partial_x T|d/2$ if the thermal flux is fixed instead), and solute by $|\partial_z S_0|H/2$, where S_0 is the initial solute distribution and is assumed to be dependent only on z. The system is then described by five dimensionless (control) parameters: the aspect ratio $A\equiv H/d$, the Prandtl number $\sigma\equiv\nu/\kappa_t$, the diffusivity ratio $\tau\equiv\kappa_s/\kappa_t$, the thermal Rayleigh number Ra $\equiv g\alpha\Delta T d^3/\nu\kappa_t$ if the temperature is kept constant at the sidewalls (or Ra$\equiv g\alpha|\partial_x T_0|d^4/\nu\kappa_t$ if the thermal flux is fixed constant instead), and the solute Rayleigh number R_s $\equiv g\beta\Delta S d^3/\nu\kappa_t = g\beta|\partial_z S_0|Hd^3/\nu\kappa_t$. [$\alpha$ is the thermal expansion coefficient, $\beta\equiv(\partial\rho/\partial S)/\rho$, and g is the gravitational acceleration.] For numerical convenience, we scale lengths in the z direction so that z lies in $[-1, 1]$, independent of the aspect ratio A. We expand the variables in truncated two-dimensional Chebyshev polynomials

$$f(x,z,t)=\sum_{i=0}^{L}\sum_{j=0}^{M} f_{ij}(t)T_i(x)T_j(z),$$

where the spectral coefficients $f_{ij}(t)$ are calculated through the cosine transform of $f(x,z,t)$ at the Gauss-Lobatto points [29]

$$f_{lm}(t)=\frac{4}{\bar{c}_l\bar{c}_m LM}\sum_{i=0}^{L}\sum_{j=1}^{M}\frac{1}{\bar{c}_i\bar{c}_j}f(x_i,z_j,t)T_l(x_i)T_m(z_j/A),$$

where $x_i=\cos(i\pi/L)$ and $z_j=\cos(j\pi/M)$ are the Gauss-Lobatto collocation points; $\bar{c}_{l(i)}=2$ if $l(i)=0$ or L, $\bar{c}_{m(j)}=2$ if $m(j)=0$ or M, and $\bar{c}=1$ otherwise. The incompressible Navier-Stokes equations under the Boussinesq approximation for this double-diffusive system thus read

$$\partial_t\vec{u}+(\vec{\nabla}\times\vec{u})\times\vec{u}=-\vec{\nabla}P+\sigma\nabla^2\vec{u}+\frac{\sigma}{16}(-RaT+R_sS)\hat{g}, \tag{2.1}$$

$$\partial_t T+(\vec{u}\cdot\vec{\nabla})T=\nabla^2 T, \tag{2.2}$$

$$\partial_t S+(\vec{u}\cdot\nabla)S=\tau\nabla^2 S, \tag{2.3}$$

$$\nabla\cdot\vec{u}=0, \tag{2.4}$$

where $\vec{\nabla}\equiv\partial_x\hat{i}+(1/A)\partial_z\hat{k}$ and $\nabla^2\equiv\partial_x^2+(1/A^2)\partial_z^2$. The boundary conditions, unless specified otherwise, are no-slip boundary conditions for the velocity ($\vec{u}=\vec{0}$) and no-flux boundary conditions for the solute ($\partial_n S=0$) at $x=\pm1$ or $z=\pm1$. The temperature may be fixed constant, or the thermal flux may be fixed constant at the sidewalls. At the top and bottom walls, we adopt insulating boundary condition: $\partial_z T=0|_{z=\pm1}$.

B. Numerical algorithms

We use an Adams-Bashforth and Crank-Nicholson scheme to evolve the system: Adams-Bashforth for the advective term and Crank-Nicholson for the Laplacian on the right-hand side [29]. After time discretization, Eqs. (2.1)–(2.3) take the general form for a time step of Δt at the $(i+1)$th iteration

$$(\nabla_n^2-\lambda)f^{i+1}=G(f^i,f^{i-1}),\quad n=1,2,3, \tag{2.5}$$

where G is a function of the variable(s) from previous time steps, $\lambda_1=2/(\sigma\Delta t)$ for Eq. (2.1), $\lambda_2=2/\Delta t$ for Eq. (2.2), and $\lambda_3=2/(\tau\Delta t)$ for Eq. (2.3). This equation is solved using the matrix diagonalization scheme [30] in 2D Chebyshev spectral space at each iteration; Δt is chosen such that the Courant criterion is satisfied at each time step. The matrix required in solving Eq. (2.5) for a given time step Δt is calculated and stored in a preprocessing routine; thus, solving this equation involves only $O(L^2M/2+LM^2/2)$ operations. The boundary conditions for each variable are incorporated in the spatial discretization using the tau approximation [29], where we first project a vector into a subspace of low-frequency components and solve for their spectral coefficients and then solve for the high-frequency components through the boundary conditions [29]. We denote this projection operation by $\mathbf{Q}_{\rm lo}$ [22], and as pointed out in [22], this operator does not commute with the spatial derivative operator $\vec{\nabla}$. This turns out to be important in implementing the influence matrix method to find the incompressible velocity, which is the subject of the following discussion.

TABLE I. Summary of the parameters and averaged length scales for the three cases. θ_0 is the angle between the steady isohaline contours and the horizontal level at the center ($x=0$), θ_1 is the averaged angle between layers and the x axis (excluding the edge cells), η_0 is the averaged layer thickness excluding the edge layers, η_1 is the averaged layer thickness including the edge layers. λ_t and λ_s are the boundary layer thicknesses determined from the horizontal gradient of temperature and salt, respectively, and λ_i is the averaged spacing between layers. The unit for the bouyancy frequency N_0 is $\sqrt{g\alpha\Delta T/d}\ \mathrm{s}^{-1}$. Note that η_0 and η_1 differ appreciably only in the case where buoyancy driving is large, so that the tilting of the edge cells is substantially greater than that of the interior cells.

	$R_\rho 10^5$	R_η	Re	N_0	$\eta\,(d)$	θ_0 (deg)	θ (deg)	$\eta_0\,(d)$	$\eta_1\,(d)$	$\lambda_t\,(d)$	$\lambda_s\,(d)$	$\lambda_i\,(d)$
Case (1)	0.7	0.29	$\sim O(10)$	$\sqrt{7}$	10/7	56.3	23.8	0.97	1.53	0.2	0.1–0.2	0.1
Case (2)	1.2	2.75	$\sim O(10)$	$\sqrt{12}$	5/6	36.6	19.2	0.40	0.49	0.2	0.1–0.2	0.1
Case (3)	1.5	5.40	$\sim O(10)$	$\sqrt{15}$	4/6	35.2	10.3	0.40	0.47	0.2	0.1–0.2	0.1

We use the multidimensional version of the influence matrix method to satisfy the divergence-free constraint [22]: we replace Eq. (2.4) with a Poisson equation for the pressure and solve for the correct pressure that will give us the divergence-free velocity. The influence matrix method allows one to find the correct pressure without advance knowledge of its boundary conditions; in other words, we look for both the pressure and its correct boundary conditions at the same time. However, a small error will occur in satisfying $\vec{\nabla}\cdot\vec{u}=0$ if the noncommutation between the two operators $\mathbf{Q}_{\mathrm{lo}}$ and $\vec{\nabla}$ is not taken care of in the implementation [22], independent of the nature of the algorithm for solving for P. Kleiser and Schumann [21] propose a remedy, called the tau correction, to remove the error due to this noncommutation. We follow the generalized version of tau correction by Tuckerman [22], but introduce a few refinements to her scheme. The first refinement is the treatment of the boundary conditions: we implement the boundary conditions into the Laplacian operator in spectral space in such a way that this spectral operator is nonsingular. This significantly reduces the ambiguity in the calculation of the inverse of the influence matrix, i.e., the determination of null vectors in the inverted influence matrix. Secondly, we use singular value decomposition (SVD), instead of eigenvalue decomposition, to calculate the inverse of the influence matrix, and also adopt the threshold for the determination of the null vectors used by Tuckerman to find the inverse of the influence matrix from SVD. We have found that, regardless of the time step and the number of modes in either direction, we always have eight null vectors for the inverted influence matrix. The calculation of the inverse of the influence matrix is very time consuming due to the complexity of the tau correction in more than one direction, and we have therefore precalculated the inverse of the influence matrix for various values of the time step and stored them for later use.

A number of authors have used the influence matrix method without the tau correction [23]; Tuckerman addressed this point [22], and Werne [31] shows the importance of the tau correction. By numerical experimentation, we confirm the conclusion in [22] that the amplitude of the divergence is independent of the number of modes used. Once we turn off the tau correction, the amplitude of the divergence of the velocity is 10^6 or more larger than the corrected one and does not decrease much as we increase the number of modes (contrary to the claims in [23]). In addition to the incompressibility constraint, another numerical challenge is the separation of spatial scales due to the different diffusivities of the diffusive species. Numerically it is not possible to carry out computations for arbitrary diffusivity ratios of the two scalar fields. The reason is that the more this ratio differs from unity, the greater is the disparity between the characteristic length scales of these two scalar fields; consequently, more grid points are needed to resolve the spatial structures. However, the heat and mass transfer across a diffusive interface are shown in experiments [32] to obey a scaling law as long as the density stratification ratio is above a critical value; no general scaling can be found for stratification ratios less than this critical value. In this paper we concentrate on quantita-tive descriptions of layer dynamics; thus we adopt a diffusivity ratio of 0.1 in our simulations.

III. CHARACTERISTIC PARAMETERS AND INITIAL STATES

A. Characteristic parameters

The previous literature of layering in both the laterally thermal driven cases and the turbulently driven cases has introduced a number of nondimensional parameters, which are very useful in characterizing the physics governing layering. In this subsection, we provide a brief summary of these characteristic parameters.

(1) $\eta\equiv\alpha\Delta T/\beta|\partial_z S_0|$. Chen, Briggs, and Wirtz [5] introduced η as a length scale for layer depth, which can also be expressed in terms of our dimensionless parameters, $\eta=A(\mathrm{Ra}/R_s)$. They obtain averaged layer thicknesses in the range of 0.6η and 0.9η [5]; Huppert and Turner reported a layer thickness of 0.66η for solute Rayleigh number $R_s\sim 10^6$ in similar experiments [33]. This length scale is the vertical distance over which the buoyancy due to horizontal temperature difference is balanced by the stabilizing solute gradient.

(2) $R_\eta\equiv g\alpha\Delta T\eta^3/\nu\kappa_t$. Chen, Briggs, and Wirtz also introduced a Rayleigh number (R_η) associated with the length scale η, which can also be expressed as $R_\eta=(\mathrm{Ra}/R_s)^3A^3\mathrm{Ra}$, it has a critical value of $(1.5\times 10^4)\pm(2.5\times 10^3)$ for the onset of layer instability, which is found to be independent of the solute diffusivity [5]. We remark here that η is a useful parameter only for layers observed in the interior because the physical circumstances governing the formation of the edge cells (top and bottom) are known to be different than for the interior [4].

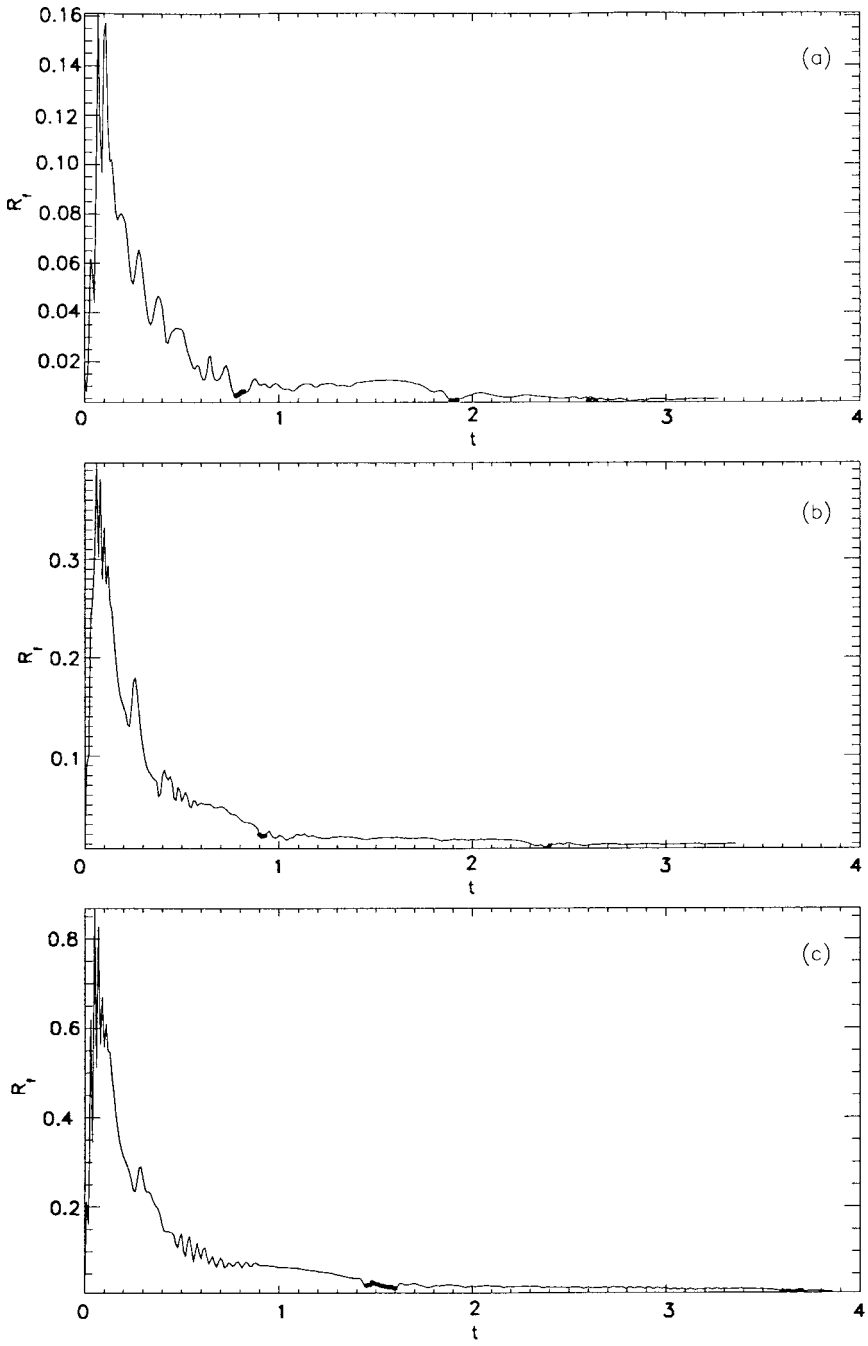

FIG. 2. Energy ratio R_f [scaled to $(\mathrm{Ra}\,\sigma A/8)$] as a function of time t; times are scaled to the slot thermal diffusion time. The three panels correspond to the three cases discussed in Sec. IV A. The oscillation at the beginning is due to the transient state as we instantly turn on the temperatures at the sidewall. In (a) [case (1)] we see well-defined peaks before $t=0.8$, when the first merging occurs at the edge cells. These peaks correspond to layer formation in the interior. (b) and (c) are the corresponding plots for cases (2) and (3), respectively. In these two cases, we do not see as many well-defined peaks corresponding to cell formation as in the first case. This is because the kinetic energy of the edge cells increases much faster in these two cases, and the ratio drops to small values at an early time. Solid dots on these curves correspond to the merging at the edge layer. The open circle in (a) indicates the interior layer merger. The small oscillations around $0.4<t<0.6$ in (b) and $0.5<t<0.8$ in (c) are due to the formation and destruction of opposite circulation cells (circulating upward at the cold end and downward at the hot end).

(3) $R_\rho \equiv \beta|\partial_z S_0|d/\alpha\Delta T$. Young and Rosner [12] introduced the density stratification ratio $R_\rho(=1/A\times R_s/\mathrm{Ra})$ to classify the various regimes in linear stability analysis. In summary, the instability is double diffusive and the shear flow is important only near the boundary for $R_\rho>1$. For $R_\rho<1$, the shear flow is dominant and the instability is shear induced. For $R_\rho<1$ our numerical simulations show cell structures similar to those in vertical slot convection [23]: cells are broken up into two pieces, which then move in opposite directions along the boundary currents. We also observe that for $R_\rho\sim 1$ two layers will be sheared horizontally in opposite directions and then merge to form a bigger cell. In our numerical simulation for the fixed sidewall temperature cases, we adopt two values of the Rayleigh numbers in the double-diffusive regime ($R_\rho \geqslant 1$), and one value in the shear driven regime ($R_\rho<1$).

(4) $\pi_3 \equiv \alpha|\partial_x T|/\beta|\partial_z S_0|$. Narusawa and Suzukawa studied layer formation due to a lateral heat flux [34], and introduced the ratio π_3 of the applied constant horizontal heat flux to the vertical solute gradient, obtaining a critical value (0.28) of this ratio for layer formation.

(5) $R_1 \equiv \alpha|\partial_x T|/(-\alpha\partial_z T_0+\beta\partial_z S_0)$. This modification of the flux ratio π_3 proposed by Schladow, Thomas, and Koseff [35] is the ratio of applied heat flux to vertical density gradient. Later Wright and Shyy [20] used $R_1 \geqslant 1$ in their numerical simulations and showed that for $R_1 \gg 1$ the horizontal intrusion is more dynamic, and merging occurs near the front of each layer at an early stage.

(6) $R_f \equiv$(integrated potential energy)/(integrated kinetic energy). In all the cases discussed above, the thermal buoyancy is the driving force that initiates layer formation. The Reynolds numbers (Ul/ν) are in the range of $\sim$10, the

buoyancy frequency $N_0 \equiv (-g\partial_z\overline{\rho}/\overline{\rho})^{0.5} \sim (R_s/\mathrm{Ra} \times g\alpha\Delta T/d)^{0.5}$ is about 0.8 s^{-1} for a temperature gradient 0.2 deg cm^{-1}, and $R_s/\mathrm{Ra}=10$ in water. In these cases layers form as a result of buoyancy balance between the destabilizing horizontal thermal gradient and the stabilizing saline gradient. In the strongly driven case, where the forcing is provided by moving a grid horizontally across the container [26,24,25], Reynolds numbers are of order several hundred, and one observes layer formation as turbulent motions are maintained by the external forcing. In these cases of stably stratified turbulent fluids, various Richardson numbers are used to qualitatively describe the system [36,37]. In our thermally driven cases, we adopt an integrated ratio, the energy density ratio R_f (similar to the flux Richardson number), to describe the mixing efficiency; R_f is defined in Eq. (4.1) below. Rather unlike the Richardson number(s), the absolute magnitude of this ratio is not related to the appearance of instability that will lead to layer formation, but it is useful as an indicator of the mixing efficiency as a function of time.

B. Initial states

There are various ways to prepare the experiments in the laboratory. In the case where the sidewall temperatures are fixed, the desired temperature difference across the walls can be established gradually (''gradual heating''). Alternatively, one can fix the sidewall temperatures to the desired values virtually instantaneously, and keep them fixed during the course of the experiments (''impulsive heating''). Chen and Chen have performed experiments [38] for both cases and found results to be similar. Kerr's linear analyses for the impulsive heating case (for large solute Rayleigh numbers) predict a layer thickness and critical temperature difference close to those for the gradual heating case [14]. In a subsequent paper he also showed that the bifurcations are subcritical (for large solute Rayleigh numbers) [15], as are those in the gradual heating case. In our simulations, we concentrate on the impulsive heating cases: We use the static state with a stabilizing salt gradient as the initial condition and instantaneously set the temperatures at the walls to the desired values. For the case where the heat flux is fixed instead, the initial state is a static state in the diffusive regime (a stably stratified density gradient with solute stabilizing and temperature destabilizing) and we instantaneously turn on the heat flux at one sidewall and keep it fixed for the rest of the calculations; this heat flux is assumed to be homogeneous on the sidewall.

IV. RESULTS

A. Fixed sidewall temperature: $A=10$, $\sigma=7$, and $\tau=0.1$

For cases where the sidewall temperature is fixed, three sets of Rayleigh numbers are used, and we observe different layer dynamics as we change the stratification ratio R_ρ. In all these computations, we use 49 modes in the x direction and 257 modes in the z direction. At $t=0^+$ the sidewall temperature is impulsively imposed. We recall that time is scaled by the thermal diffusion time across the slot, and the time step is usually as small as 10^{-4} to maintain stability in the temporal integration. As we turn on the sidewall temperatures, cells near the ends are observed to form first and a weak circulation is found in the interior; the top edge cell forms near the cold wall while the bottom edge cell forms near the hot wall. The interior circulation is weak as the isohaline contours adjust to the relaxing temperature profile and a steady circulation is established before any instability grows. (The circulation at the center of the slot corresponds to the background state in the linear analysis.) Within the edge cell the solute is well mixed and the temperature is rendered stable. As edge cells grow and advance toward the interior, the vertical thermal and solute gradients are found to accumulate at the layer boundaries. Instability in regions next to the edge cells is thus initiated (see [13]), and two cells are found to form simultaneously next to the edge cell. Of these two cells, the one immediately adjacent to the edge cell has opposite circulation (downward near the hot wall and upward near the cold wall) to the dominant circulation direction in the slot and soon dies. The other cell, with the same orientation as the edge cells (upward near the hot wall

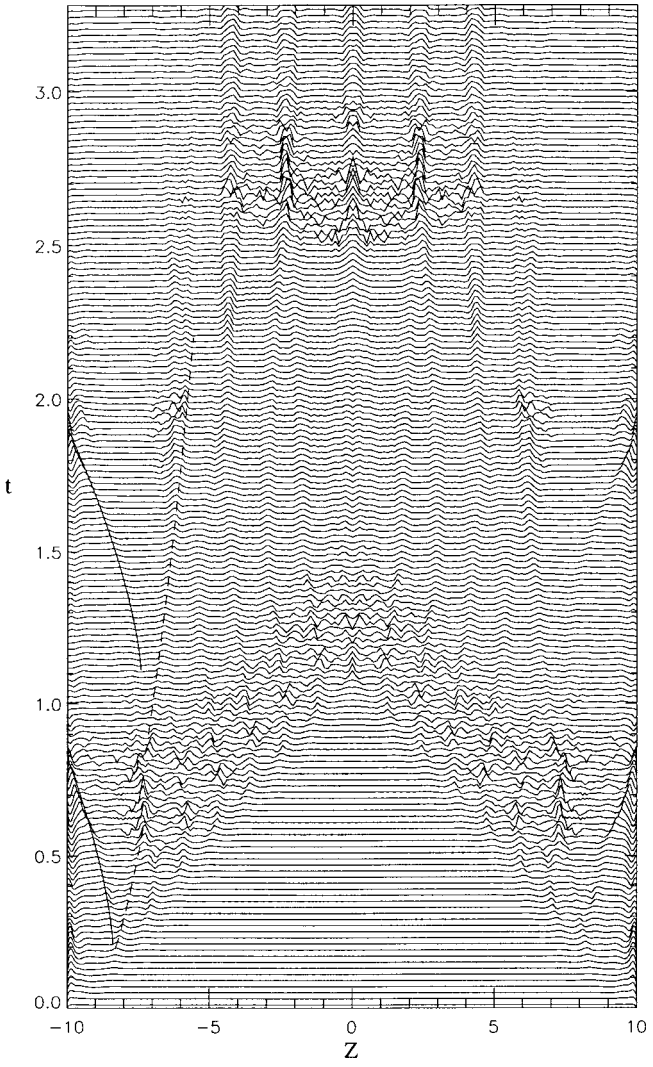

FIG. 3. Average buoyancy gradient $\overline{\nabla}_{\mathrm{buoy}}$ as a function of z and t for case (1). The dashed lines are fits to the trajectories of the in-moving boundary of the edge cell. They are proportional to $t^{0.5}$. The solid lines are fits to the trajectories of the outward-moving boundary of the neighboring cells, soon to be swallowed by the edge cell. They are proportional to $(t-t_0)^{1.5}$, where t_0 is a free parameter. These two dashed lines have different proportionalities.

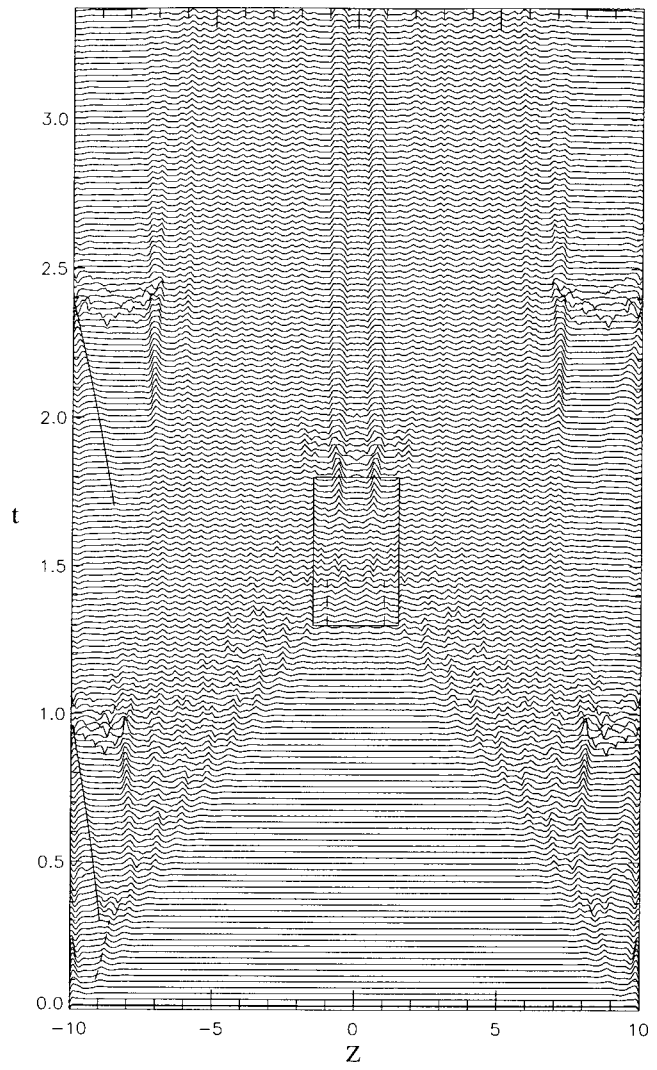

FIG. 4. Time-space plot of $\overline{\nabla}_{\text{buoy}}$ for case (2). In this case we can fit the trajectory of the advancing boundary of the edge cell to the $t^{0.5}$ curve only before the first encounter with the neighboring cell. The boxed area is where cells disappear due to the decreasing buoyancy gradient; no merger occurs in this region.

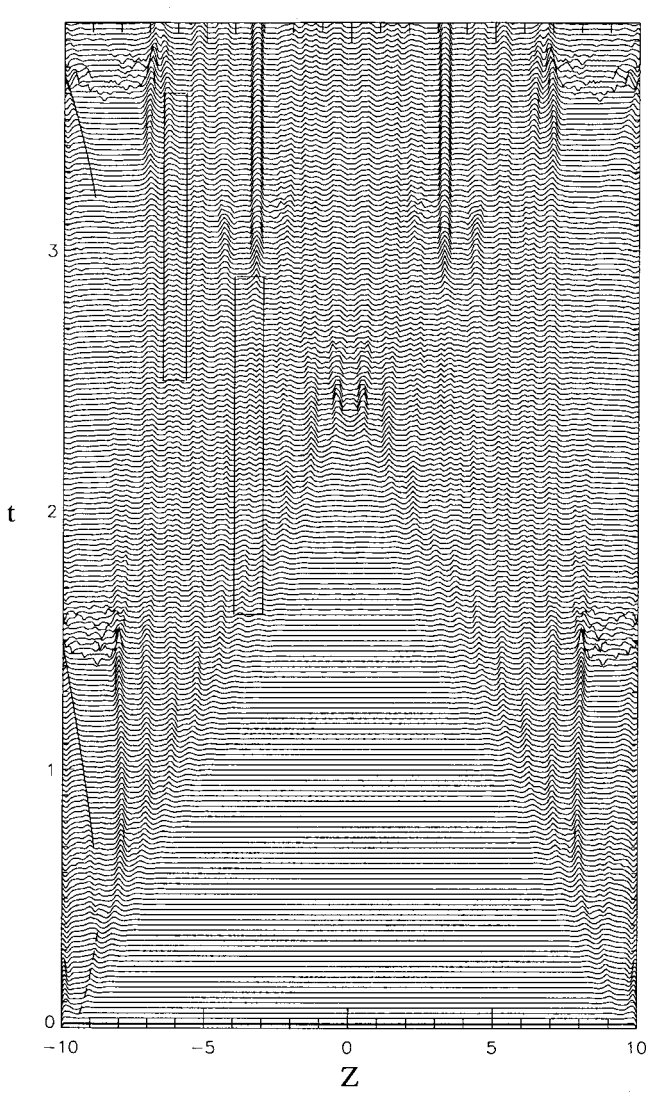

FIG. 5. Time-space plot of $\overline{\nabla}_{\text{buoy}}$ for case (3). We note that in this case the layer dynamics evolves more slowly than in the first two cases. The two boxes enclose regions where cells disappear as the buoyancy gradients fail to sustain layer structures. The differences found in these two regions are discussed in the text (See. V).

and downward near the cold wall), survives and grows in size and initiates cell formation next to it. This process continues until layer formation reaches the center. In the interface regions between the layers, the stabilizing salt gradient increases as a result of mixing within cells. The calculations also show that the vertical thermal gradient is rendered destabilizing in these interfaces while the density is rendered stably stratified. In the following, we shall use the energy density ratio (similar to the flux Richardson number defined in [26]) to describe the mixing efficiency, and the buoyancy gradient to describe the layer dynamics. We also present several horizontally averaged quantities as functions of z and t for three sets of Rayleigh numbers (Ra,R_s), all with $A=H/d=10$, $\sigma=7$, and $\tau=0.1$: (1) $(\mathrm{Ra},R_s)=(8.6\times10^4, 6.1\times10^5)$, (2) $(\mathrm{Ra},R_s)=(1.6\times10^5,1.92\times10^6)$, and (3) $(\mathrm{Ra},R_s)=(1.6\times10^5,2.4\times10^6)$. These parameters correspond to a temperature difference of $\Delta T=2°-4°$ in water if the width of the slot is about $d=1.9-2.5$ cm. In the first case $(R_\rho=0.7)$ the boundary currents along the vertical walls are strong, and cells are tilted by these boundary currents as they form; after layer formation we observe interior cells merging to form a single cell which is twice the size of the original one (see Sec. V for details). In this case, the calculation is carried to 3.5 thermal diffusion times. For cases (2) and (3), $R_\rho>1$ and the salt stratification can prevent the vertical shear from destroying layer structures; calculations are carried to 4 thermal diffusion times. For water ($\nu=0.01\,\mathrm{cm^2\,s^{-1}}$ and $\nu/\kappa_t=7$) this corresponds to observing the experiment for 0.5–1.5 h with $d=2-2.5$ cm.

In Table I we list parameters of interest and summarize the various averaged length scales from the simulations for the three cases. We note that the tilting angles are averaged over all cells except for the top and bottom (edge) cells in all cases. In addition to the parameters introduced in Sec. III, we also include five length scales and two angles as described in the table caption.

We first examine the effect of cell creation and destruction on the overall efficiency of convection. To do this, we define the integrated energy density ratio as

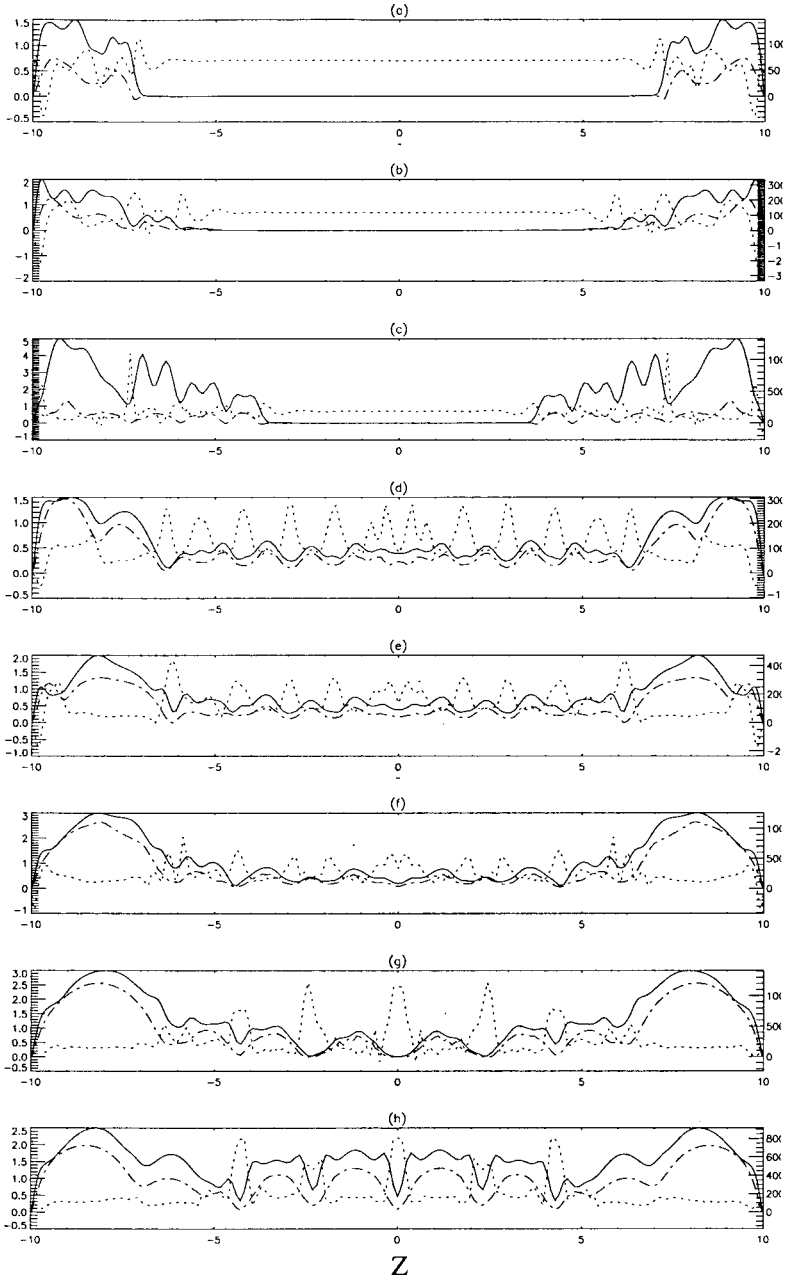

FIG. 6. Horizontally averaged kinetic energy density ($\overline{e}$, solid line), buoyancy flux ($f_{\mathrm{buoy}}/2$, dash-dotted line), and buoyancy gradient ($\overline{\nabla}_{\mathrm{buoy}}$, dotted line) as functions of z at eight different times for case (1). $t=0.3$, 0.5, 0.7, 1.5, 1.7, 2.0, 2.5, and 3.28 for plots (a)–(h), respectively. The left ordinate is for both $\overline{\nabla}_{\mathrm{buoy}}$ and $f_{\mathrm{buoy}}/2$; the right ordinate measures the scaled kinetic energy density $\overline{e}$.

$$R_f \equiv \frac{\int -gz(-\alpha T+\beta S)\,dx\,dz}{\int (u^2+w^2)\,dx\,dz} = \frac{\mathrm{Ra}\,\sigma A}{8}\,\frac{\int z(T-R_s/\mathrm{Ra}\,S)\,dx\,dz}{\int (u^2+w^2)\,dx\,dz}, \tag{4.1}$$

where the integral is taken over the whole box. We plot $R_f/(\mathrm{Ra}\,\sigma A/8)$ as a function of time in Figs. 2(a)–2(c) for the three cases. We remark that in our simulations, where the flow is driven by a lateral temperature difference, R_f can be very large at the beginning since we start from a virtually static state where the potential energy is much greater than the kinetic energy. The inverse of R_f measures the efficiency of conversion from potential energy to kinetic energy. We see that R_f does not vary smoothly in time, and that it varies by orders of magnitude as the potential energy is converted to kinetic energy during layer formation and merging.

We utilize horizontally averaged quantities to describe layer dynamics as in [27]. The horizontally averaged buoyancy gradient (in nondimensional form) $\overline{\nabla}_{\mathrm{buoy}}(z,t) \equiv (g\alpha\Delta T/Ad)^{-1} g(\alpha\overline{T}_z-\beta\overline{S}_z)=\overline{T}_z-(R_s/\mathrm{Ra})\overline{S}_z$ is a good indicator of the layer dynamics [26,27]: spikes in the buoyancy gradient vertical profile correspond to layer locations as can be seen in Figs. 3–5 where we plot $\overline{\nabla}_{\mathrm{buoy}}(z,t)$ as a function of t and z for the three cases. One concern might be that the layer tilting in our case might cause difficulties in defining physically meaningful horizontal averages. The reason that layer tilting does not make much of a difference to our argument is as follows: As we take the horizontal average near a tilted layer boundary, we pick up contributions from the two layers on either side of the boundary. However, the difference in height due to this tilting never exceeds $\frac{1}{5}$ of the layer thickness for the internal layers in all cases, so that the total contribution from adjacent layers is localized near their

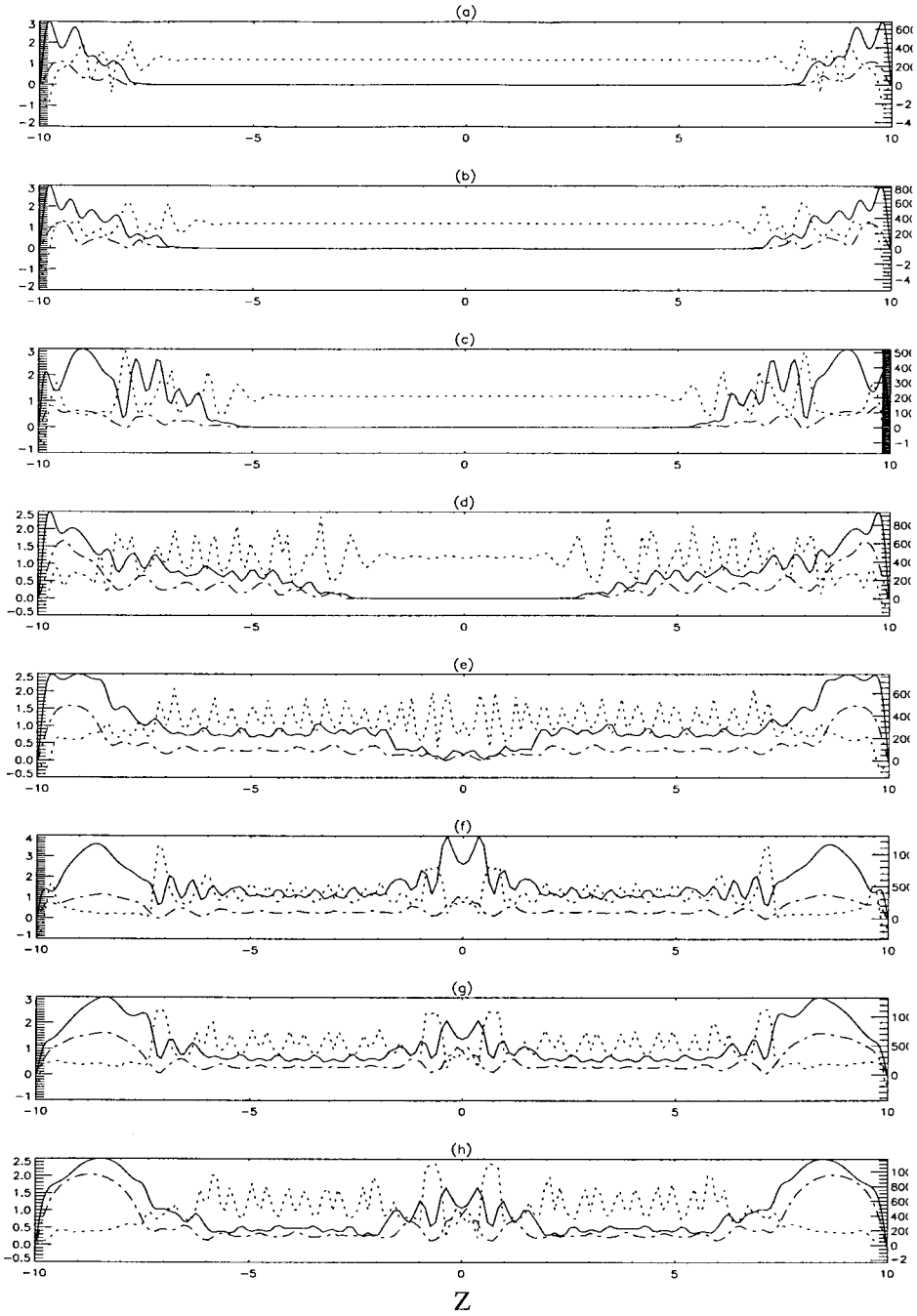

FIG. 7. Snapshots of kinetic energy density ($\overline{e}$, solid line), buoyancy flux ($f_{\text{buoy}}/2$, dash-dotted line), and buoyancy gradient ($\overline{\nabla}_{\text{buoy}}$, dotted line) as functions of z at eight different times for case (2). $t=0.35$, 0.5, 0.7, 1.1, 1.5, 2.2, 2.5, and 3.36 for plots (a)–(h), respectively. Coordinate axes have the same meaning as in Fig. 6.

common boundary. Furthermore, the no-flux and no-slip boundary conditions at the sidewalls enhance the peak values in the mean buoyancy gradient and buoyancy flux at the center of the layer boundaries. Since our argument does not depend on the actual values of the horizontally averaged quantities, but instead only on the vertical position of their extrema (which are known to mark the boundaries), we need only check if the positions of these extrema indeed correspond to the boundary positions. We have therefore compared the position of layers determined from the mean quantities to 2D results from our simulations, and find that the correspondence between the position of the extrema of the mean buoyancy gradient and buoyancy flux and the position of the midpoint of the tilted boundary layers is excellent.

As shown in [26], merger events are manifested as the ''collision'' of spikes in $\overline{\nabla}_{\text{buoy}}(z,t)$. For example, consider the evolution of spikes in Fig. 3: at $t\sim 0.35$, two spikes are generated at $z=\pm 8.5$, moving toward $z=\pm 10$, respectively. These outward-moving spikes are the retreating ends of the edge layer boundaries: as the bottom (top) edge cell advances on the hot (cold) end and retreats on the cold (hot) end, the neighboring cell is pushed toward the retreating end, moving downward toward the cold wall (upward toward the hot wall for the top edge cell). At $t\sim 0.8$ (when the outward-moving spikes hit the wall) the edge layer completely swallows the neighbor cell and continues expanding until it swallows another cell at $t\sim 1.6$. These outward-moving spikes follow trajectories proportional to $t^{1.51}$ from $t\sim 0.4$ to $t\sim 0.8$ (the solid line in Fig. 3). For $0.2<t<0.5$ and $0.8<t<1.8$, the inward-moving spikes travel along curves proportional to $t^{0.5}$, denoted by the dashed lines in Fig. 3 (see [27] for comparison.) At $t\sim 1.2$ we have altogether 14 layers; at

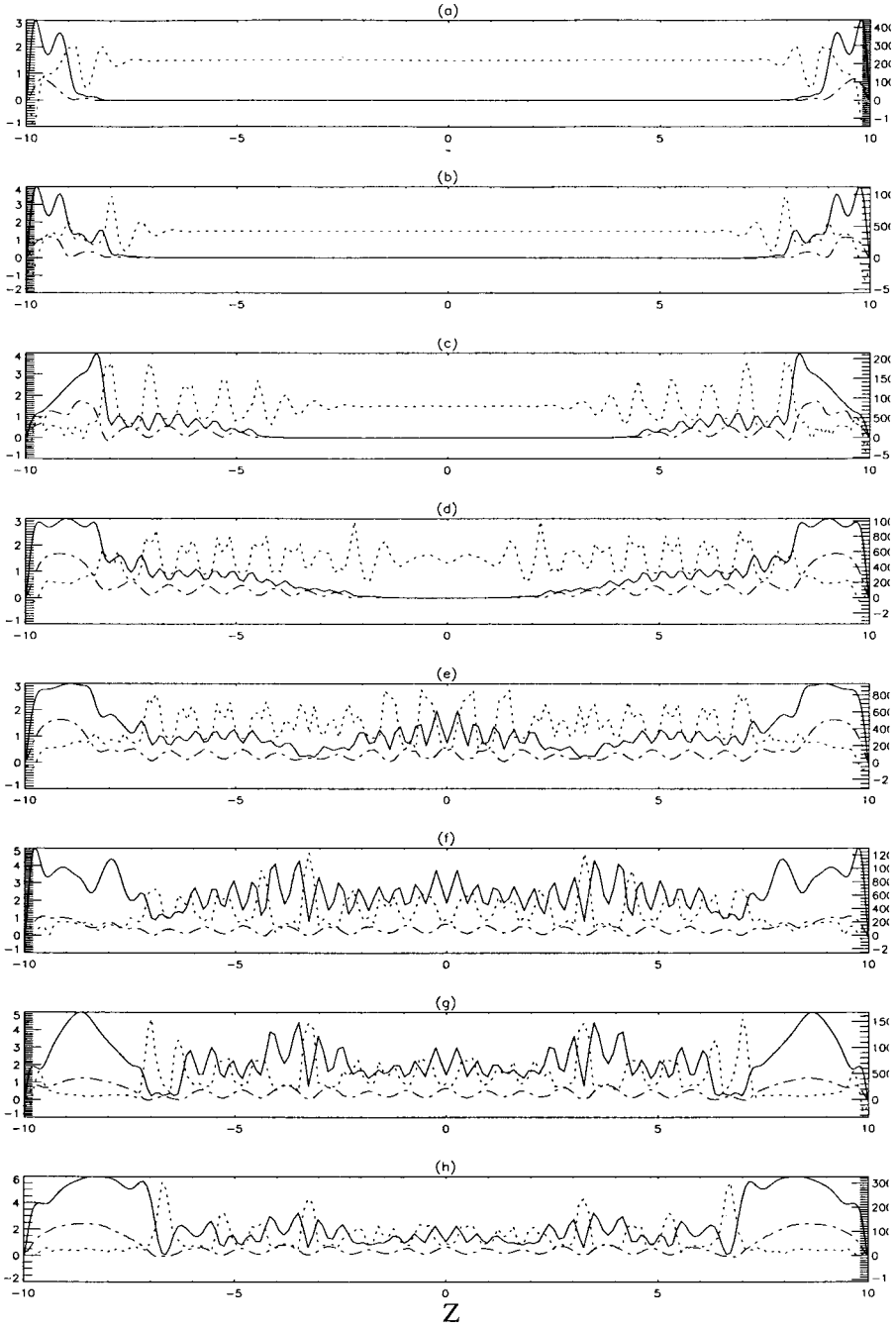

FIG. 8. Snapshots of kinetic energy density ($\overline{e}$, solid line), buoyancy flux ($f_{\text{buoy}}/2$, dash-dotted line), and buoyancy gradient ($\overline{\nabla}_{\text{buoy}}$, dotted line) for case (3). $t=0.35$, 0.6, 1.5, 2.0, 2.5, 3.0, 3.5, and 3.86 for plots (a)–(h), respectively. Coordinate axes have the same meaning as in Fig. 6.

$t\sim 1.6$, the two edge layers swallow their neighbor cells again to form bigger cells, leading to 12 cells; from $t\sim 1.7$ onward merging occurs over the entire container (to be described in Sec. V) and lasts until $t\sim 2.5$, when only 7 layers remain. The edge layers continue to work their way toward the center, swallowing the neighboring cells until the end of our calculation. For the other two cases (Figs. 4 and 5), the advancing front of the edge cells follows the $t^{0.5}$ trajectory (dashed line) until the edge cells swallow their neighbor cells. The outward-moving spikes in these two figures (solid curves) also follow the $t^{1.5}$ trajectory (as in case 1) until they hit the end walls.

The average (dimensionless) buoyancy flux $\overline{f}_{\text{buoy}}(z,t) \equiv (g\alpha\kappa_t\Delta T/d)^{-1} g(\alpha\overline{wT}-\beta\overline{wS}) = \overline{wT}-(R_s/\text{Ra})\overline{wS}$ is observed to have the same layer structures as those of the buoyancy gradient. In Figs. 6–8 we display the average buoyancy flux, together with the buoyancy gradient and the average kinetic energy density $\overline{e}\,[\equiv(\overline{u^2+w^2})/2$, scaled to $(2\kappa_t/d)^2]$ at eight different times. We note that the buoyancy flux $\overline{f}_{\text{buoy}}$ reaches a minimum wherever the buoyancy gradient $\overline{\nabla}_{\text{buoy}}$ reaches a maximum (and vice versa), and that $\overline{f}_{\text{buoy}}$ does not go to a constant value after the merging, in contrast to the results in [27].

The (dimensionless) salinity difference across the box and its vertical gradient, $h(z,t)\equiv(\rho_0\alpha\Delta T)^{-1}\rho_0\beta S(x,z,t)|_{x=-1}^{x=1} = (R_s/\text{Ra})S(x,z,t)|_{x=-1}^{x=1}$ and $\partial_z h(z,t)$, are also good indicators of layer boundaries. We show contour plots of both $h(z,t)$ and $\partial_z h(z,t)$ for the three cases in Figs. 9, 10, and 11, respectively. As cells develop, the solute is homogenized by the circulation inside the cell and accumulates near the layer boundaries, where the vertical velocity is zero. In panels (a)

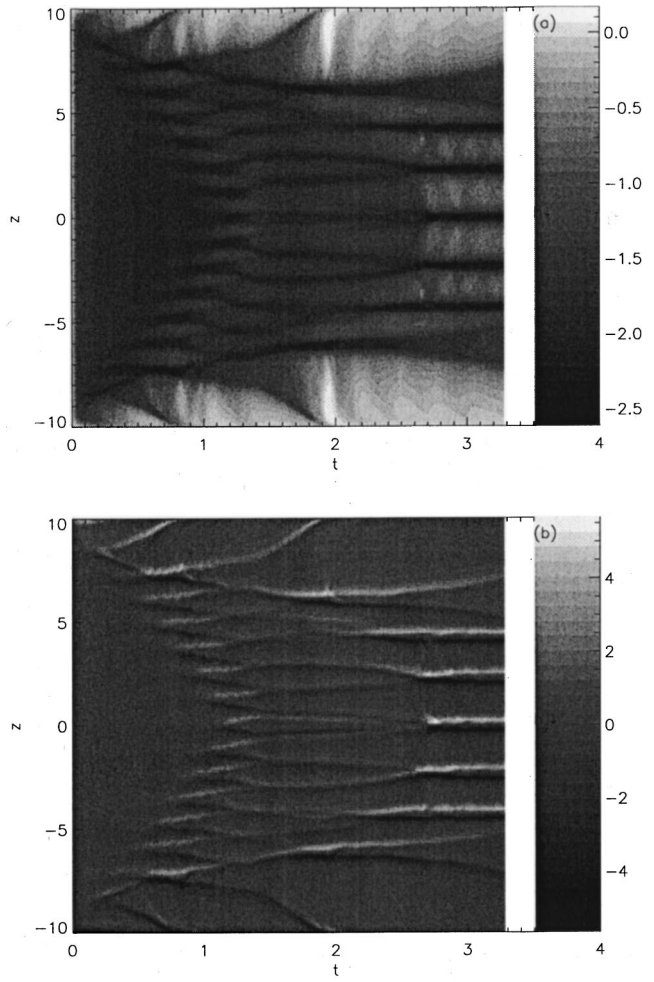

FIG. 9. (a) Horizontal salinity difference (h) across the box as a function of z and t in gray scale for case (1). (b) Vertical gradient of the horizontal salinity difference ($\partial_z h$) for case (1). The gray scale color tables are shown next to the right ordinate in both panels.

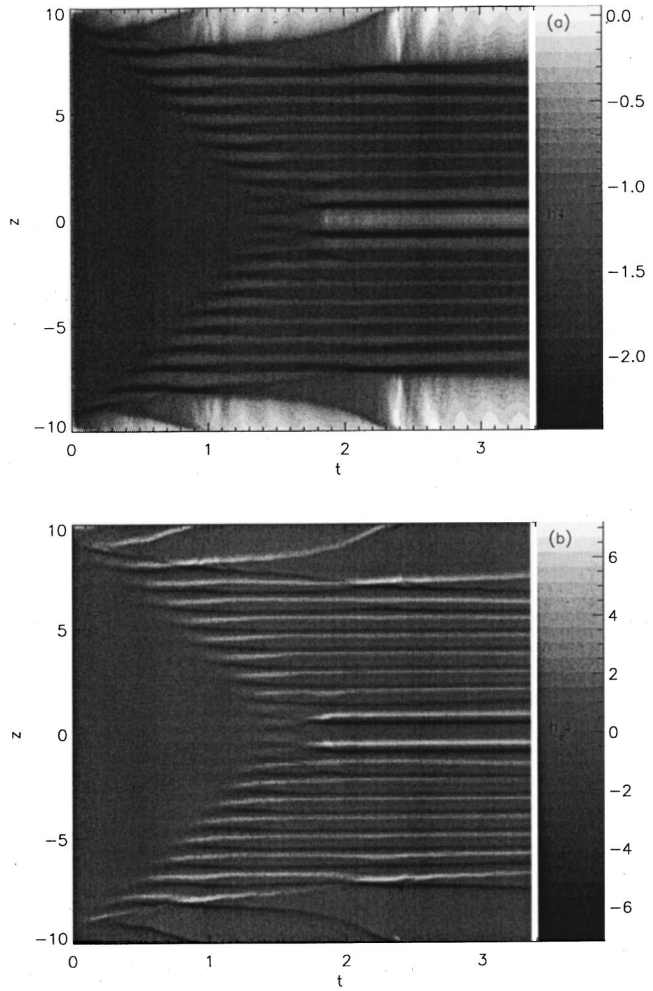

FIG. 10. (a) Horizontal salinity difference across the box as a function of z and t in gray scale for case (2). (b) Vertical gradient of the horizontal salinity difference for case (2). The gray scale color tables are shown next to the right ordinate in both panels.

of Figs. 9–11, the darker stripes correspond to the layer boundaries and the lighter stripes correspond to circulation inside the cell where solute is redistributed. First, we note that at $t \sim 0.6$ in Fig. 9 a horizontal solute gradient is found near the center as a steady flow is established in the interior, and h remains constant there until layers form. Second, we note that the larger the stratification ratio, the longer it takes for layers to develop and to mix the solute; this effect is evidenced by noting the time it takes for the dark stripes to turn gray. In panels (b) of Figs. 10 and 11, each pair of adjacent stripes (one lighter and one darker) corresponds to one layer boundary in the isohaline contour plots: the lighter stripe corresponds to the position of the boundary at the hot wall, while the darker stripe corresponds to the position of the boundary at the cold wall. In Fig. 9(b), the contrast between these two stripes in a pair is not large until merging occurs. As cells undergo merging, the solute contrast becomes larger, and thus h increases in amplitude at first. As the mixing is enhanced, h is homogenized (decreased in amplitude) within the merging cell, and rapidly accumulates near the layer boundaries; that is why the contrast of $\partial_z h$ increases after merging.

We next consider the results for heat and solute transport. In Figs. 12(a)–12(c) we show contour plots of horizontally averaged vertical heat fluxes as functions of z and t for the three cases, respectively; we scale the (dimensionless) heat flux $\vec{F} = \vec{u}T - \vec{\nabla}T$ to the horizontal conductive heat flux ($\kappa_t \Delta T/d$ in this case). Initially, the sidewall temperatures are set instantaneously to fixed values, and thus heat is transported by the interior circulation in the slot. As temperature relaxes toward the steady profile in the interior (at the center, this steady state is the background state in the linear analyses [12]), the vertical heat flux decreases everywhere except near the end walls, where cells grow and the heat flux is enhanced by convection. A dramatic increase in the amplitude of the thermal flux is observed as layers merge. This transient behavior leads to almost an order of magnitude change in the heat flux for the edge cells as they swallow the neighbor cells. As layer formation proceeds toward the center of the box, the vertical heat flux first increases in amplitude within the cells, oscillates for a while, and then decreases if no merging occurs.

We see that most of the heat supplied from the sidewalls is advected to the edge cells (confirming an earlier conjecture by Thorpe, Hutt, and Soulsby [4]) by comparing Fig. 12 with the temporal evolution of the Nusselt number Nu shown in Fig. 13; the latter quantity is just the scaled horizontal heat

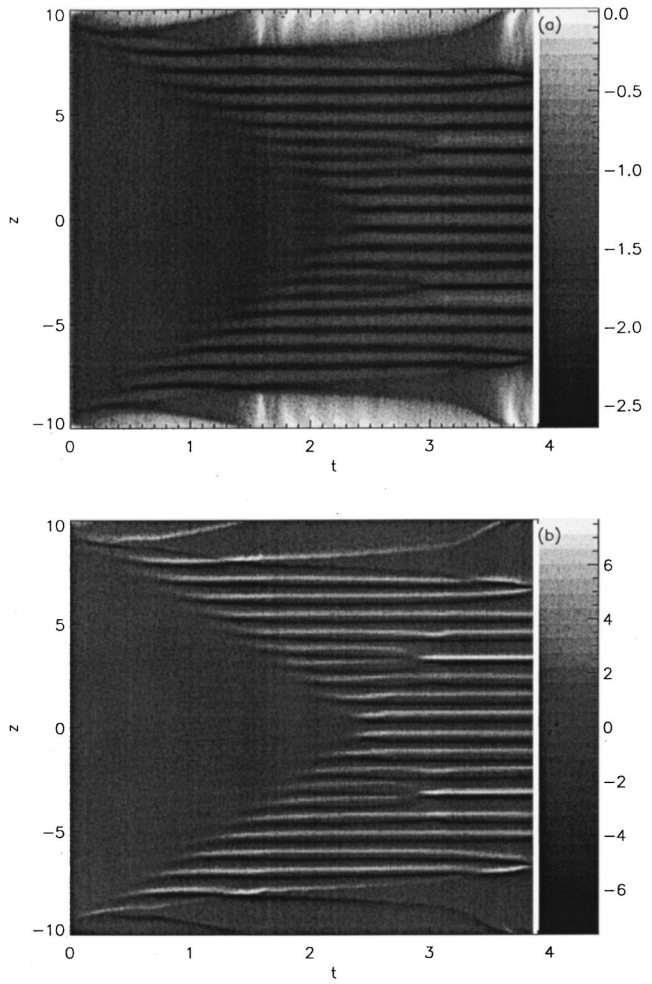

FIG. 11. Horizontal salinity difference h (a) and its gradient $\partial_z h$ (b) in gray scale for case (3). The gray scale color tables are next to the right ordinates in both panels.

flux averaged over z at the hot wall, $\mathrm{Nu} \equiv \int (uT - \partial_x T)_{x=-1} dz / \int dz$. The salt flux is generally more enhanced than the heat flux when merging occurs, as seen in Figs. 14(a)–14(c): these panels show the horizontally averaged salt flux $\vec{F}^s$, scaled to the conductive vertical heat flux ($-\kappa_s \partial_z S_0$ in this case), $\vec{F}^s = A(\vec{u}S/\tau - \vec{\nabla}S)$, as functions of z and t for the three cases, respectively.

One notices that after merger events, both the salt and heat fluxes decrease faster than the kinetic energy flux, as can be seen in temporal and vertical profiles of the horizontally averaged kinetic energy flux shown in Figs. 15(a)–15(c).

We also observe oscillations in the heat, salinity, and kinetic energy fluxes after a layer merger occurs. These oscillations are manifested by the alternating colors seen after merging events in Figs. 12, 14, and 15. These oscillations are closely related to thermal waves seen to propagate from one sidewall to the other near the top and bottom of the newly formed cells after merger.

B. Constant lateral heat flux: $A = H/d = 2$, $\sigma = 7$, and $\tau = 0.1$

Narusawa and Suzukawa [34] observed layer formation as a constant lateral heat flux is applied to a body of fluid characterized by a stably stratified solute; and Schladow, Thomas, and Koseff [35] observed layers when the stabilizing solute was accompanied by a destabilizing temperature gradient. In order to investigate layer dynamics in this case, we fix on a particular set of values for the control parameters: we assume an aspect ratio $A = 2$, a Prandtl number $\sigma = 7$, a diffusivity ratio $\tau = 0.1$, $(\mathrm{Ra}, R_s) = (2.4 \times 10^5, 3.2 \times 10^6)$, and a constant lateral heat flux $\partial_x T = 24 \partial_z T_0$ at $x = -1$, where $\partial_z T_0$ is the initial temperature gradient. These choices correspond to $R_1 = 2$ and $\pi_3 = 1.8$ (as defined in Sec. III). The initial state is assumed to be static, with a destabilizing temperature gradient and a stabilizing solute gradient.

At $t = 0$, the lateral heat flux is turned on and is kept constant for the rest of the calculation. At onset, cell formation occurs very quickly. Thus, by the time $t \sim 0.3$, we find that eight dominant cells have already formed, with an average layer depth of $\sim 0.2d$. Between these dominant cells we also observe five smaller counter-rotating cells; some of these grow for a short while, and three of these decay as cells of the dominant circulation orientation (upward near the hot wall and downward near the cold wall) grow. The dominant cells also evolve: some simply die away, while others merge as in the case of fixed sidewall temperatures. Thus, near the end of our simulation, only four dominant cells and two counter-rotating cells remain, with an average layer depth of $\approx 0.5d$.

The evolution of the dominant circulation cells can be described in more detail as follows. The temperature near the top wall increases very rapidly from onset, while the temperature near the bottom wall increases much less rapidly. As a consequence, the vertical thermal gradient is rendered stable over the entire slot by $t \sim 0.4$. During this period, the top cell expands (by virtue of the fact that its bottom boundary moves downward), and the bottom cell contracts (by virtue of the fact that its upper boundary also moves downward); the displacement of the bottom of the top cell scales as t^1 (shown as the dashed line in Fig. 16), while the displacement of the top of the bottom cells is much faster, and scales as $t^{1.5}$ (shown as a solid line in the same figure). The scaling of the top boundary of the bottom cell is thus identical to that for the outward-moving spikes in the constant sidewall temperature case.

In the present case we also see layers merge during this early period, and also observe decay of cells in the middle of the simulation domain. Layers merge in similar fashion to the layer merging seen in the constant sidewall temperature cases: heavy cells roll on top of light cells, the two merging rapidly due to overturn instability (see Sec. V).

An important aspect of the constant lateral heat flux case is that it shows spike collisions that do not correspond to cell mergers. An example is shown in the boxed area of Fig. 16, which shows the collision of two spikes, leading to the generation of a single spike. Examination of the temporal evolution of either the flow field or the salinity difference h and its vertical gradient $\partial_z h$ (shown in Fig. 17) shows that this spike collision corresponds to the decay of a cell, together with the growth of an adjacent cell into the space vacated by the decaying cell: no cell merger is involved. Thus, figures such as Fig. 16 are insufficient by themselves to distinguish between cell mergers, and cell death and growth.

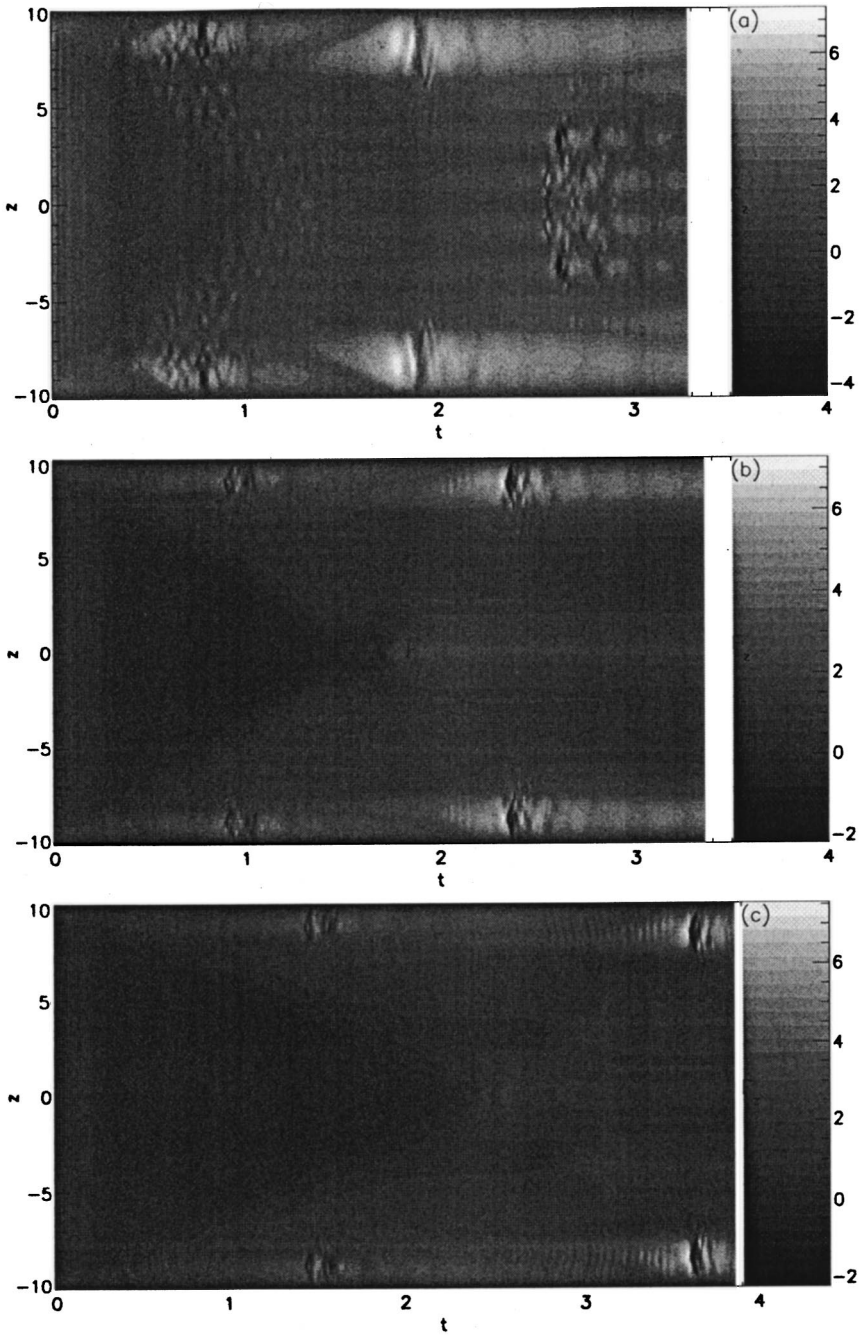

FIG. 12. Horizontally averaged vertical heat flux $\overline{F_z}$ as a function of z and t for the three aspect ratio 10 cases, (a)–(c), respectively. The gray scale color tables for F_z are shown next to the right ordinates. We observe a drastic change in the amplitude of F_z as two cells merge in all three cases.

Finally, examination of the kinetic energy density ($\overline{e}$), three horizontally averaged vertical fluxes ($\overline{F_z}$, $\overline{F_z^s}$, and $\overline{f_e}$), buoyancy gradient ($\overline{\nabla}_{\text{buoy}}$) and buoyancy flux ($\overline{f}_{\text{buoy}}$) shows very similar behavior to that observed in the constant sidewall temperature case: we see bursts and subsequent oscillations in the vertical fluxes as two cells merge; and that the buoyancy flux is not spatially uniform (in Fig. 7) after cell merger.

V. DISCUSSION AND SUMMARY

A. Layer formation and dynamics

In this section, we focus on the layer dynamics via the horizontally averaged equations for the buoyancy. We remark again that, though the mean quantities have contributions from both cells across the tilted boundaries, they serve well to represent the layer structures because the tilting does not affect the correspondence in vertical location between the extrema in the horizontally averaged quantities and the layer boundary midpoints. Through the horizontally averaged equation for the kinetic energy density and global energy balance equation in our case, we relate our system to Balmforth, Smith, and Young's model [27] for layering in the case of stirred stably stratified fluids [26,25,37].

In order to understand the processes leading to layering, we first develop the horizontally averaged equation for the buoyancy. If we define the dimensionless buoyancy (scaled by $g\alpha\Delta T/2$) by $\overline{b}\equiv\overline{T}-(R_S/\mathrm{Ra})\overline{S}$, average Eqs. (2.2) and (2.3) over x, multiply the averaged Eq. (2.3) by R_S/Ra, and subtract the resultant equation from the averaged Eq. (2.2), we obtain the horizontally averaged equation for the buoyancy,

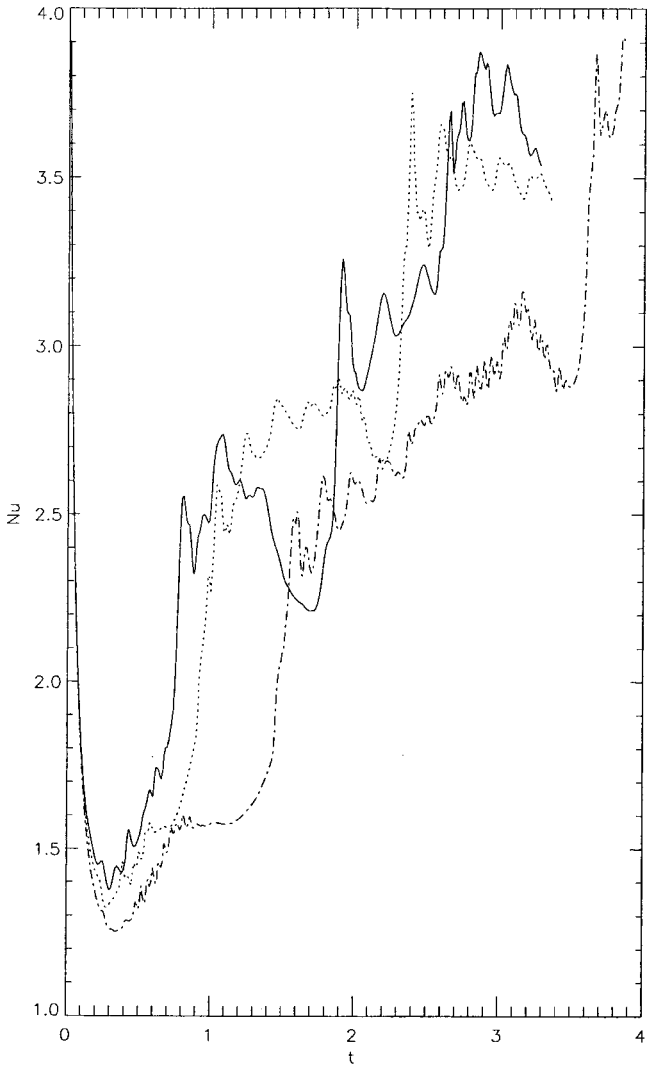

FIG. 13. Vertically averaged Nusselt number Nu (evaluated at the hot wall, $x=-1$) as a function of time. Solid line: case (1); dotted line: case (2); dash-dotted line: case (3). We observe that Nu increases rapidly whenever layer merger occurs.

$$\partial_t \overline{b} + \frac{1}{A}\partial_z \overline{f}_{\text{buoy}} = \frac{1}{A}\partial_z \overline{\nabla}_{\text{buoy}} + \tfrac{1}{2}\,\partial_x T\big|_{x=-1}^{x=1} + \frac{R_s}{\text{Ra}}(1-\tau)\frac{1}{A^2}\partial_z^2 \overline{S}, \tag{5.1}$$

where $\overline{f}_{\text{buoy}}$ and $\overline{\nabla}_{\text{buoy}}$, as defined in Sec. IV, are the buoyancy flux and buoyancy gradient, respectively. Equation (5.1) can be used to understand much of the dynamics of layer formation and evolution. The effect of different diffusivities is manifested by the last term on the right-hand side of this equation: it vanishes if $\tau=1$, and for cases of interests ($\tau<1$; in our simulations, $\tau=0.1$), $(1-\tau)\sim 1$. The net horizontal heat flux $\partial_x T|_{x=-1}^{x=1}$ is the driving force. As the linear instability sets in, the horizontal thermal gradient builds up a buoyancy flux $\overline{f}_{\text{buoy}}$, and a vertical buoyancy gradient accumulates near the horizontal interfaces between cells as a result of the flow pattern in the cell. As long as $\tau\neq 1$, $\overline{\nabla}_{\text{buoy}}$ and $\partial_z^2 \overline{S}$ soon dominate the right-hand side as the staircase structures form. Since in our case the temperature serves only as a perturbing force ($R_s/\text{Ra}>1$), layers remain steady if the flow within cells reaches a steady pattern. However, in the case of small stratification ratios ($R_\rho<1$), the newly formed layers cannot reach a steady state due to the strong vertical boundary currents; as a consequence of the boundary currents, these cells move upward at the hot wall and downward at the cold wall, and we observe formation of separatrixes in the interior cell circulation (a higher mode in the x direction)—each cell subsequently breaks into two small subcells, moving in opposite directions along the vertical shear flow. Still later we observe cell deformation, interior mergers, and formation of bigger cells as described in Sec. V B. The evolution of the edge cells is also a case in which steady state cannot be reached, even for $R_s/\text{Ra}>1$. In this case, the cell neighboring the bottom edge cell constantly advects solute toward the edge cell (an analogous process happens at the top); this advection accelerates the edge cell's circulation (because it converts potential energy to kinetic energy), and leads to an upward extension of the upper boundary of the edge cell, i.e., the edge cell grows in size. Thus the buoyancy flux provides ''momentum flux'' for the edge cells to propagate toward the center.

In the case of constant lateral heat flux, we observe similar layer dynamics: the contribution from the constant lateral heat flux initiates layer formation, and more solute accumulates near the cell boundary as cells develop. However, in this case, all the cell boundaries propagate downward and the temperature rises much faster at the top than at the bottom.

There are two important key features in the flux-gradient relation in Balmforth's model: (1) the buoyancy flux increases once the buoyancy gradient becomes sufficiently large, which captures the steepening of the interface; and (2) there exists an intermediate range of buoyancy gradients for which the flux decreases (increases) as the gradient increases (decreases), which mathematically well poses the model. From our numerical simulations the buoyancy flux-gradient dependence in our case can be summarized as follows: First, we found that for both interior and edge cells, $\overline{f}_{\text{buoy}}$ is not a single-valued function of $\overline{\nabla}_{\text{buoy}}$ as in [27]. The multivaluedness seen in our results may be due to the fact that different regions in the cells undergo different instabilities. Second, we also observe a range of buoyancy gradients for which layer-forming instability occurs ($\mathcal{F}'<0$ in [27], where the buoyancy flux decreases as the buoyancy gradient increases). Third, there exists a range of values for the buoyancy gradient for which the buoyancy flux increases as the buoyancy gradient increases (as long as both are sufficiently large); this range is larger for the edge cells than for the interior cells, which may explain why the edge cells keep advancing toward the interior.

Finally, we note that the arguments presented for layering in stirred stably stratified fluids by [27] carry through even more extensively than might be expected by comparison of our Eq. (5.1) (on which our above discussion of layering is based) and Eq. (2.1a) of Balmforth, Smith, and Young [27]: indeed, we can derive equations for the horizontally averaged kinetic energy density and a global energy equation similar to Eqs. (2.1b) and (2.2) of [27]. For example, we derive the equation for the horizontally averaged kinetic en-

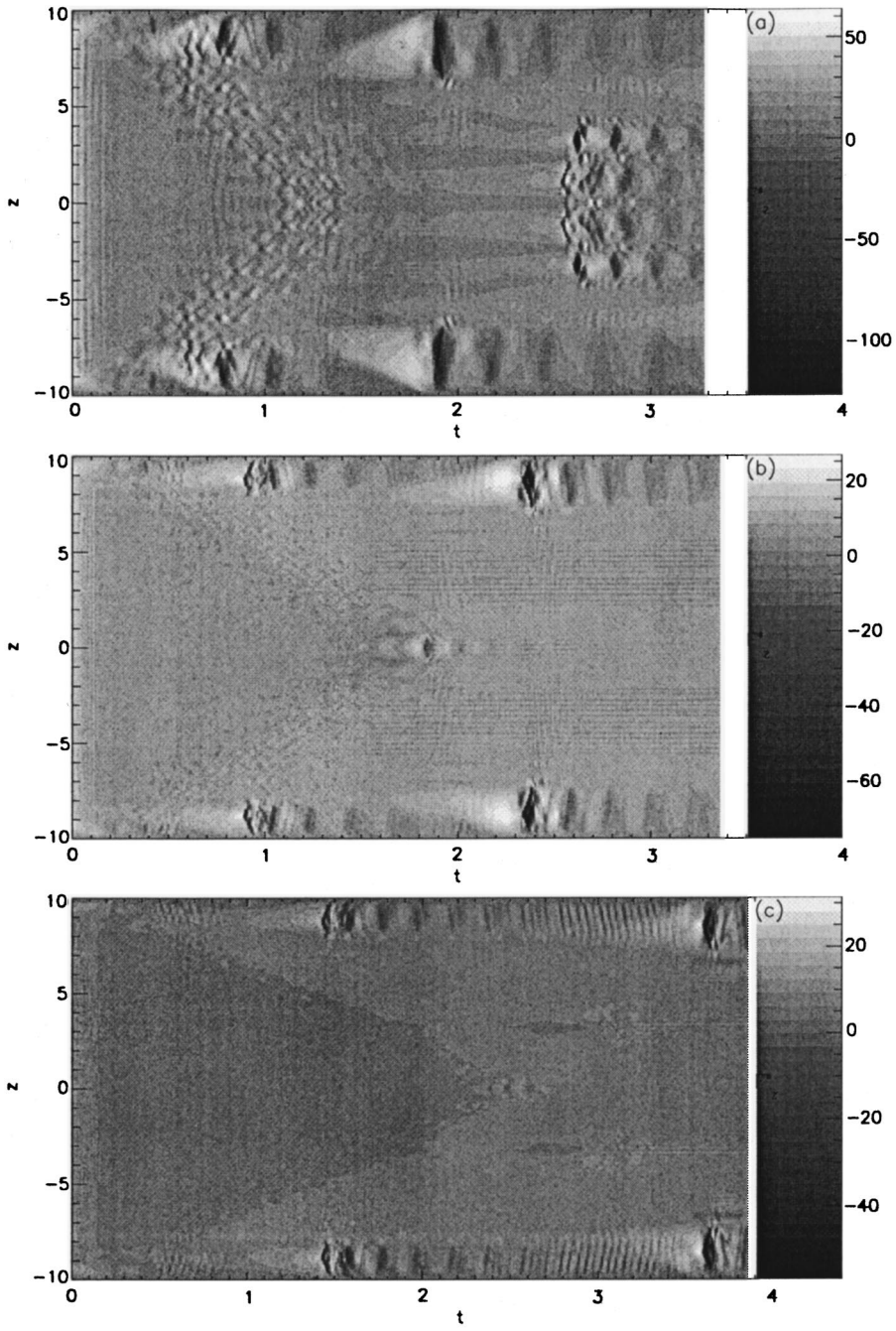

FIG. 14. Horizontally averaged vertical salt flux $\overline{F_z^s}$ as a function of z and t for the three aspect ratio 10 cases [(a), (b), and (c)]. The gray scale tables for $\overline{F_z^s}$ are shown next to the right ordinates. We observe more oscillations in the interior when cells form in case (1) (from $t=0.5$ to $t=1.2$). These interior oscillations are associated with the wobbling observed in the streamlines. As the stratification ratio is increased (R_ρ) in cases (2) and (3), we see lower-amplitude oscillations (and hence less wobbling in the streamlines). This oscillation is responsible for the tilting of the cells (in all three cases), and is closely related to the later interior cell merger in case (1) (for details, see Sec. V). We also observe oscillations in the edge cells after merging (Sec. V).

ergy density [$\overline{e}$ scaled by $(2\kappa_t/d)^2$] by taking the inner product of Eq. (2.1) with $\vec{u}$ and averaging the result over x, obtaining

$$\partial_t \overline{e} = \frac{1}{A}\partial_z\left(\frac{\sigma}{A}\partial_z \overline{e} - \overline{wP} - 2\sigma\overline{u\partial_x w}\right) + \frac{\sigma\,\mathrm{Ra}}{16}\overline{f}_{\mathrm{buoy}} - \sigma\overline{\Omega^2}, \tag{5.2}$$

where P is the pressure in Eq. (2.1) and $\Omega \equiv \partial_z u - \partial_x w$ is the vorticity. [Note that we have assumed incompressibility, no-slip boundary conditions for the velocity, and no-flux boundary conditions for the solute in the derivations of Eqs. (5.1) and (5.2); we further note that we can obtain the same equations if the no-slip boundary conditions at the sidewalls are replaced by stress-free boundary conditions.]

The equation for the global energy balance of the system can be derived by combining Eqs. (5.1) and (5.2) to obtain the nondimensional result

$$\begin{aligned}\partial_t \int_{-1}^{1}\left(\overline{e} - A\frac{\mathrm{Ra}\,\sigma}{16} z\overline{b}\right)dz &= \frac{\sigma}{16A}\left[\mathrm{Ra}\,\overline{T} - R_s\tau\overline{S}\right]_{z=-1}^{z=1} - \int_{-1}^{1}\sigma\overline{\Omega^2}\,dz \\ &\quad - \int_{-1}^{1} A\frac{\mathrm{Ra}\,\sigma}{16}\frac{z\partial_x T|_{x=-1}^{x=1}}{2}dz.\end{aligned} \tag{5.3}$$

In the derivation of this energy balance equation, the term $(1/A)\partial_z \overline{f}_{\mathrm{buoy}}$ in Eq. (5.1) cancels with $(\sigma\,\mathrm{Ra}/16)\overline{f}_{\mathrm{buoy}}$ in Eq.

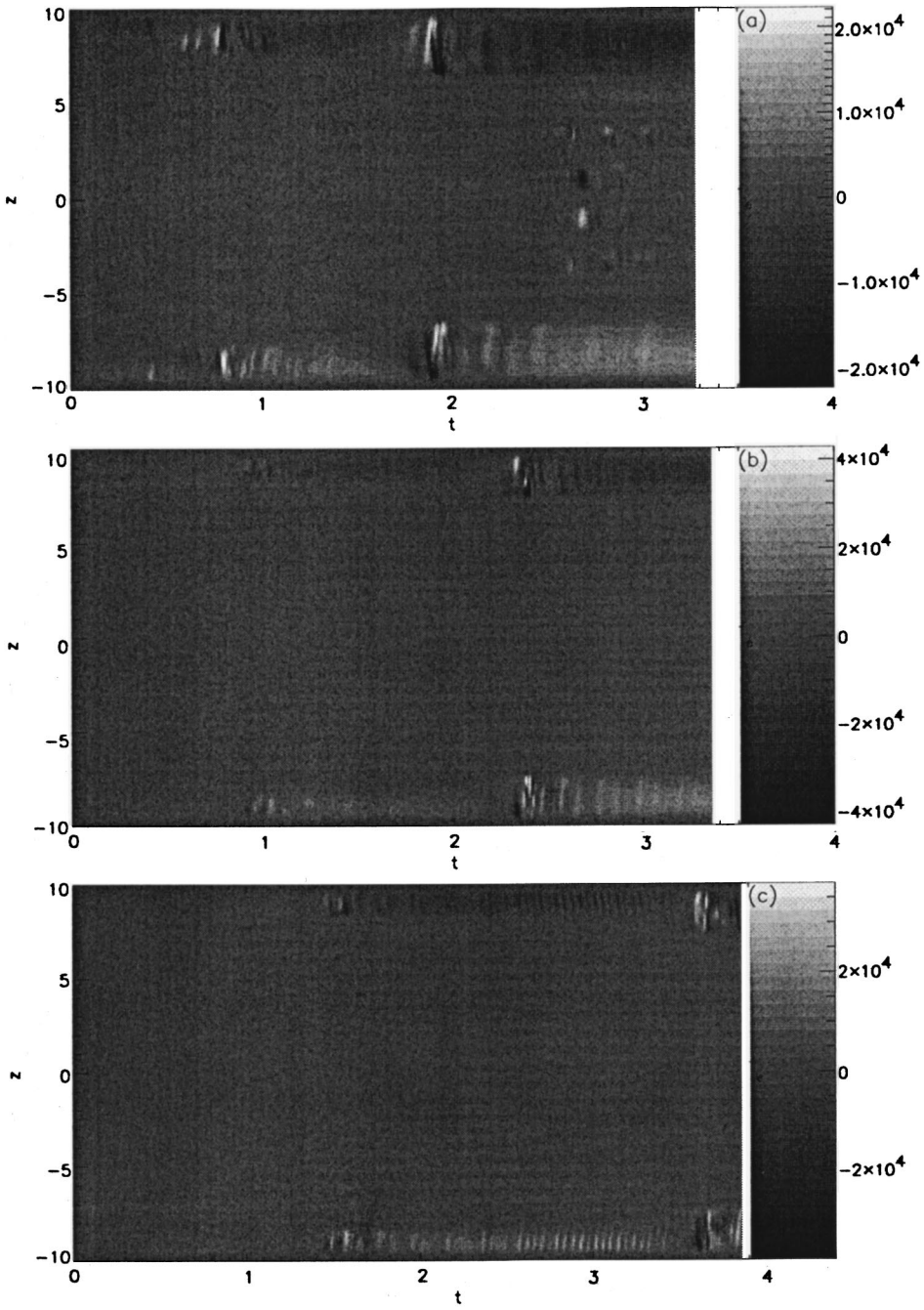

FIG. 15. Horizontally averaged vertical kinetic energy flux ($\overline{f_e} \equiv \overline{w(u^2+w^2)/2}$) as a function of z and t for the three aspect ratio 10 cases [(a), (b), and (c)]. The gray scale tables for $\overline{f_e}$ are shown next to the right ordinates. We observe oscillations in the edge cells after merging.

(5.2); we obtain the prefactor of the potential energy term $z\overline{b}$ in the above integral by dividing $(Ad/2)g\alpha\Delta T/2$ by $(2\kappa_t/d)^2$. This equation thus balances the rate of change of the total energy of the system [the term on the left-hand side of Eq. (5.3)] with the total potential energy available in the system (the first term on the left-hand side), the (always negative) energy dissipation rate associated with vorticity generation, and (finally) the net lateral heat flux, which is the source and sink of the total energy and thus is the external driver of this system. (Note that the adopted boundary conditions do not allow kinetic energy and buoyancy to enter or leave the system via the end walls.)

Equations (5.2) and (5.3) resemble the corresponding Eqs. (2.1a), (2.1b), and (2.2) in [27] if we identify the vorticity term with the turbulent energy dissipation term $\epsilon l^{-1}\overline{e^{3/2}}$ on the right-hand side of Eq. (2.9b) in [27] (l is the mixing length and ϵ is a nondimensional mixing-length parameter related to the stratification strength in the formulation of [27]). In Eqs. (5.2) and (5.3), the kinetic energy diffuses through viscous dissipation and hence the coefficient (fluid viscosity scaled to thermal diffusivity) is a constant in front of the vorticity term. (In contrast, in the cases of stratified turbulent fluids, one adopts eddy viscosity for this kinetic energy dissipation term because the characteristic length scale of the average kinetic energy is determined by both the length scale of the stirring device and the stratification.)

Thus, we see that our horizontally averaged equations are virtually identical to those of Balmforth, Smith, and Young [27], with the principal difference lying in the nature of the forcing: in our case, the motions are buoyancy driven, whereas in their case, motions are driven by external forcing. Thus, while the mixing length (l) is determined by both the

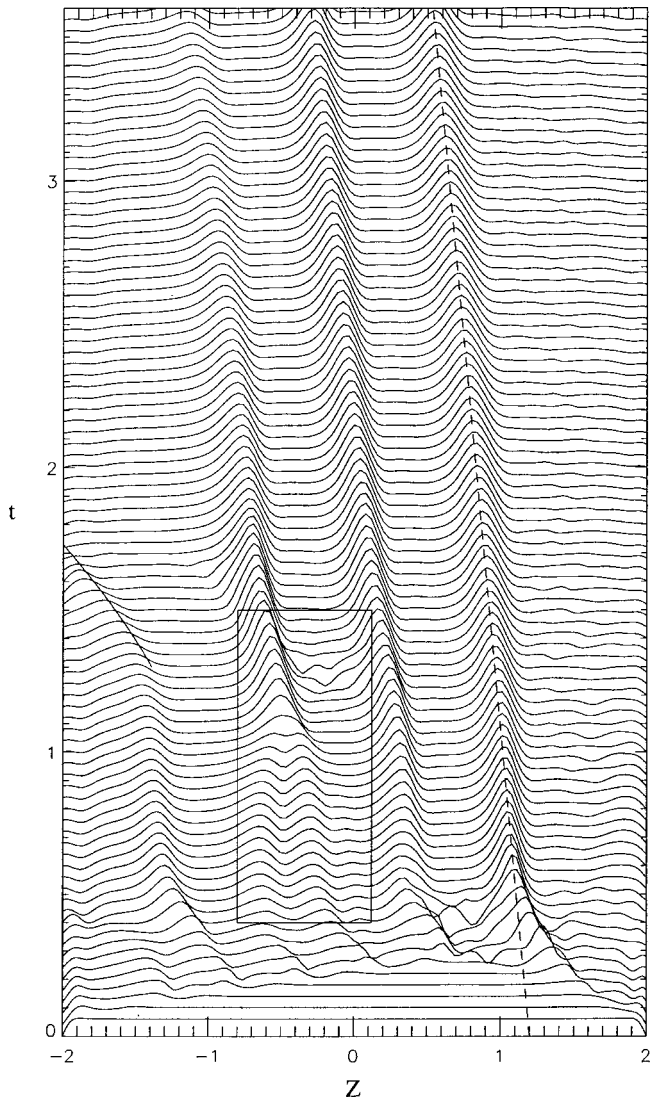

FIG. 16. Time-space plot of $\overline{\nabla}_{\text{buoy}}$ for the constant lateral heat flux case. The dashed line traces the trajectory of the layer boundary of the top cell; unlike the $t^{0.5}$ fit in the constant sidewall temperature cases, here the fit is proportional to t. The solid line shows the $t^{1.5}$ fit to the trajectory of the outward-going spike. Within the box around $z=-0.6$ a cell decays as another cell (around $z=-0.3$) grows. At $t=1.2$ a cell grows around $z=-0.2$; it is soon swallowed by the cell it grows in. We also note the wavy behavior of $\overline{\nabla}_{\text{buoy}}$ in the top cell ($1.2<z<2.0$).

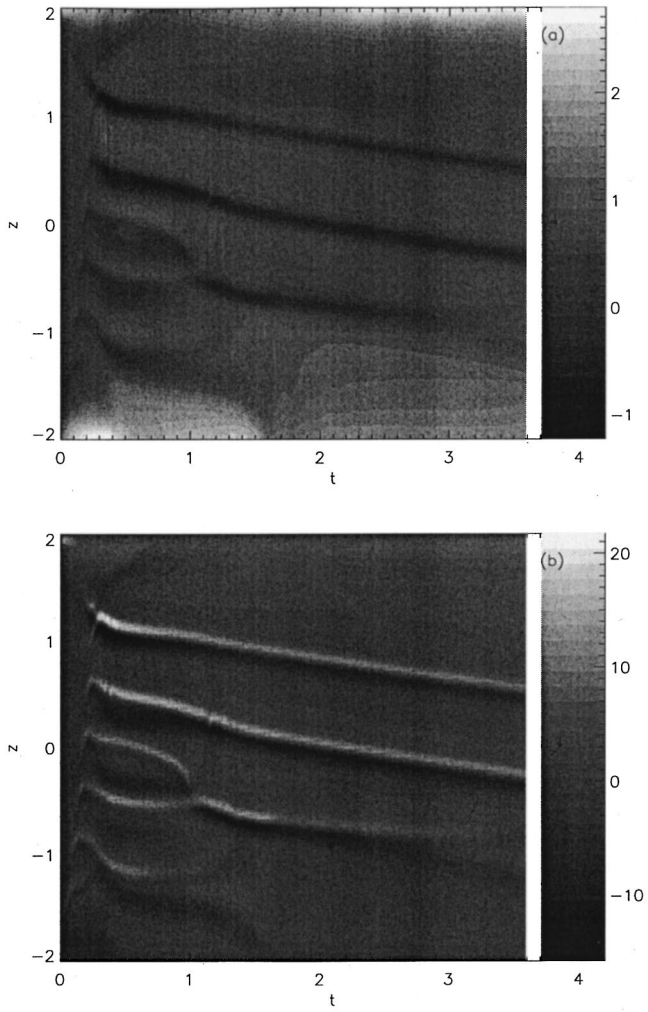

FIG. 17. (a) Salinity difference (h) across the box for the constant lateral heat flux case. Again, dark stripes correspond to layer boundaries, where both horizontal salinity difference and its gradient accumulate. (b) $\partial_z h$ as a function of t and z.

stirring device and the stratification in [27], in our case the corresponding scale length emerges from the linear stability. Nevertheless, their physical arguments (related to the balance between the buoyancy gradient and the buoyancy flux) seem to carry over to our problem, and can provide a physical explanation for the observed layering under these apparently very different physical circumstances.

B. Merging and decay of cells

In this section, we provide a factual description of cell merger and decay, focusing on the physical circumstances that appear to control merger and decay. We confine our discussion to the constant boundary temperature case, for which the aspect ratio is 10.

During the merging of two layers, we observe hot and salty fluid sinking as cold and fresh fluid floats up near the center of the merging site. As two cells merge, the lower (heavier) cell moves upward, turns over, and lies on top of the upper (lighter) cell. As a result, the density is unstably stratified (top heavy), the fluid undergoes Rayleigh-Taylor instability, and potential energy is converted to kinetic energy in a burstlike fashion. Due to this potential energy release, more slat is advected as the cell circulation speeds up. (We note in passing that in our simulations, the density is never rendered stably stratified after two vertical cells interchange positions, so that we do not expect finger instability to set in to enhance the transport of both salt and heat, as seen by Lambert and Demenkow [39].)

Figures 18 and 19 show a series of pictures as merging of two layers takes place. For edge cell merging (Fig. 18), the advancing layer boundaries directly cause merging: The horizontal temperature difference causes the edge layer boundary to tilt as it grows; for the top edge cell, the advancing end is along the cold wall where circulation moves toward the center and the retreating end is along the hot wall, and vice versa for the bottom edge cell. As the boundary tilts, the neighboring cell is squeezed toward the retreating

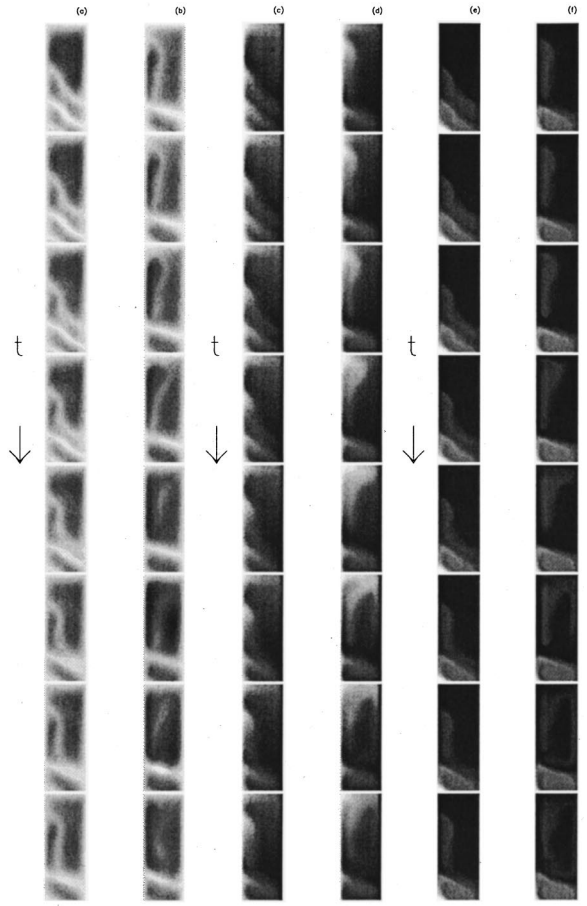

FIG. 18. Time series of the top edge cell merging with the neighbor cell. (a) and (b) are gray scale contours of the stream function, (c) and (d) are isothermal contours, and (e) and (f) are isohaline contours. For each box in the panels, the width is d and the height is approximately $2.6d$ (this aspect ratio is the same in all the plots). In this gray scale representation, white is hot and heavy, and dark is cold and fresh. We can see that the neighbor cell moves toward the retreating end of the edge layer boundary; this neighbor cell becomes hotter (white) as it moves up. Because it is heavier (white), it sinks as it reaches the cold wall.

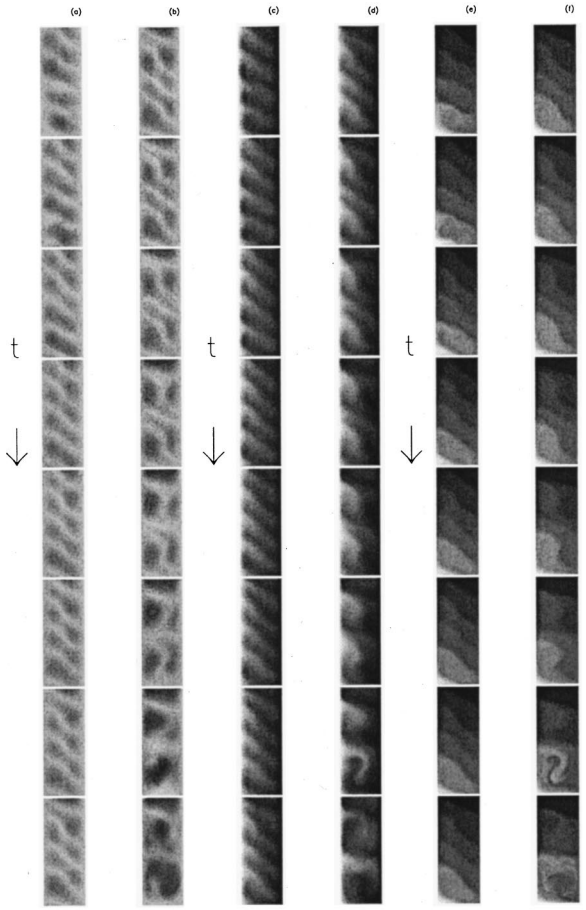

FIG. 19. Time series of interior cells merging. (a) and (b) are gray scale contours of the stream function, (c) and (d) are isothermal contours, and (e) and (f) are isohaline contours. For each box in the panels, the horizontal dimension is d and the vertical dimension is approximately $2.6d$. As in Fig. 18, white is hot and heavy, and dark is cold and fresh.

end of the edge cell, and these two cells merge as soon as part of the well-mixed heavier cell lies on top of the lighter cell [40–42].

For interior layer merging (Fig. 19), numerical simulation shows that the stratification ratio plays an important role. As the interior cells grow, we observe oscillation of the cells in the horizontal direction. This oscillation (wobbling) subsides as the cell expands and homogenizes the horizontal temperature and saline gradients. If the solute stratification is large ($R_\rho \geqslant 1$), the interior layers remain steady after the wobbling ceases. In cases (2) and (3) ($R_\rho > 1$) some layers disappear as nearby cells have larger buoyancy gradients (and thus more robust layer structures). These disappearing ''weak'' layers (with weak buoyancy gradients to sustain the layer boundaries) decay as the nearby cells expand with well-defined cell structure; no merging occurs in these cases (see the boxes in Figs. 3–5). However, for case 1 where the stratification ratio $R_\rho < 1$, the wobbling serves to seed the instability of higher-order modes in the interior flow. Thus, the evolution of interior layers is as follows: First we observe cells to wobble as they develop. As the wobbling initiates instability in the horizontal direction, we observe formation of separatrixes in the streamlines in the cells. Two small subcells are found in the interior cells, circulating in the same orientation. These two small cells have the same solute concentration but different temperature distribution. As these two closed subcells form, the layer boundaries of these interior cells tilt upward at the hot end and downward at the cold end, and one of the subcells dies as the other keeps expanding. As one of the subcells grows at one end, the lower and upper neighbor cells are forced to expand at the opposite end. As the dying subcells vanish, a pair of interior neighbor cells begin to move toward each other: the upper cell moves downward and the lower cell moves upward. Soon these two cells (growing in size at different ends) circulate around each other. Overturn instability occurs as the heavier cell is dragged on top of the lighter one by the boundary shear flow. Potential energy is released as the top-heavy cell sinks down, and a large cell of twice the size of the original cell is formed. The generation of separatrixes of the streamlines in the interior cells may be due to the instability of higher modes in the x direction, initiated by the wobbling of the streamlines. We also observe separatrix formation in cases where the instability is shear driven ($R_\rho \ll 1$). In those cases,

each interior cell is torn into two cells and moves along the boundary currents. Thus this kind of merging process is not seen when the stratification ratio is large ($R_\rho > 1$), where the shear flow is much weaker near the boundary and the instability is double diffusive in nature.

Finally, we comment on the decay of cells, as observed in cases (2) and (3) for aspect ratio 10. The boxes shown in Figs. 4 and 5 are regions where decay of interfaces occurs. Two cells form almost simultaneously at $z=-0.5$ and $z=-1.0$, respectively, around $t\sim 1.3$ (Fig. 4). The one near the center has larger buoyancy gradient to start with, and keeps expanding as the neighbor cell decays. This is illustrated as the breakup of a weak spike into smaller ones along the dashed lines in the box in Fig. 4. In case (3) (Fig. 6) we observe a similar occurrence of layer decays in the box near $z=-3.5$. However, in the box close to $z=-6.5$ the decaying spike on the right does not break into small spikes, but instead decays while the left spike increases its amplitude as a result. In Fig. 16 we observe two spikes colliding at $z=-0.5$ around $t=1.1$; however, this is not a merger event. The cell at $z=-0.2$ expands faster than the one at $z=-0.6$, which eventually decays as the cell at $z=-0.2$ keeps expanding.

C. Summary

We have simulated vertical double-diffusive convection in a confined, elongated container. We start with a static initial state with a stably stratified solute gradient; the sidewall temperature is then turned on impulsively at the beginning of the calculation. We have performed three sets of simulations for the constant sidewall temperature, aspect ratio 10 cases, and concluded that the stratification ratio (R_ρ) is important in characterizing the interior layer dynamics. For $R_\rho < 1$, the tilting of the interior layer boundaries is strong enough to deform the cells into two subcells. Two neighbor cells merge as the heavier subcell lies on top of the lighter one. During the merging, overturn instability takes place and the potential energy is released in a bursty manner. For $R_\rho > 1$, we observe layers to decay as the neighbor cells expand and no interior merging is observed throughout the computation.

We have described layer dynamics via the use of horizontally averaged variables. For example, the layer boundaries are manifested by spikes in the mean buoyancy gradients. By comparing the mean buoyancy gradient with the two-dimensional stream functions, we are able to distinguish collision of spikes in the mean buoyancy associated with merger events from those due to the decay and expansion of cells. We also applied arguments for layer formation in [27] (the flux-gradient relations) to our cases, and found some similarities as well as differences. In all the cases, the edge cells expand toward the center of the box in a similar fashion to that found in [27]. This similarity in behavior may be due to the similarity in the equations describing the averaged variables and the fact that identical vertical boundary conditions were adopted for the buoyancy gradient and kinetic energy density gradient. From the evolution of the heat transport we conclude that most of the heat flux applied to the sidewalls to maintain the constant sidewall temperatures goes to the edge cells, confirming a previous conjecture by Thorpe, Hutt, and Soulsby [4].

Finally, we have also simulated the constant lateral flux case, and have found that, except for the fact that there is a preferred direction for the layers to propagate due to the increasing vertical thermal gradient, the layer dynamics and the transport of heat and solute are similar to those in the case of constant sidewall temperature.

ACKNOWLEDGMENTS

We would like to thank N. Balmforth, J. Biello, F. Cattaneo, T. Dupont, K. Julien, N. Lebovitz, L. Tuckerman, J. Werne, and W. Young for helpful conversations. This work was supported by the NASA Space Physics Theory Program and DOE/ASCI Center grants at the University of Chicago.

[1] J. S. Turner, *Buoyancy Effects in Fluids* (Cambridge University Press, Cambridge, 1973).
[2] J. S. Turner and H. Stommel, Proc. Natl. Acad. Sci. USA **52**, 49 (1964).
[3] J. S. Turner, J. Fluid Mech. **33**, 183 (1968).
[4] S. A. Thorpe, P. K. Hutt, and R. Soulsby, J. Fluid Mech. **38**, 375 (1969).
[5] C. F. Chen, D. G. Briggs, and R. A. Wirtz, Int. J. Heat Mass Transf. **14**, 57 (1970).
[6] J. E. Hart, J. Fluid Mech. **49**, 279 (1971).
[7] C. F. Chen, J. Fluid Mech. **63**, 563 (1974).
[8] J. E. Hart, J. Fluid Mech. **59**, 47 (1973).
[9] C. F. Chen, J. Fluid Mech. **63**, 563 (1974).
[10] R. C. Paliwal and C. F. Chen, J. Fluid Mech. **98**, 769 (1980).
[11] S. Thangam, A. Zebib, and C. F. Chen, J. Fluid Mech. **112**, 151 (1981).
[12] Y. Young and R. Rosner, Phys. Rev. E **57**, 1183 (1998).
[13] Y. Young and R. Rosner, Phys. Rev. E **57**, 5554 (1998).
[14] O. S. Kerr, J. Fluid Mech. **207**, 323 (1989).
[15] O. S. Kerr, J. Fluid Mech. **217**, 529 (1990).
[16] R. A. Wirtz, D. G. Briggs, and C. F. Chen, Geophys. Fluid Dyn. **3**, 265 (1972).
[17] R. A. Wirtz, Int. J. Heat Mass Transf. **20**, 841 (1977).
[18] J. C. Heinrich, Int. J. Numer. Methods Eng. **20**, 447 (1984).
[19] J. W. Lee and J. M. Hyun, Int. J. Heat Mass Transf. **34**, 2409 (1991).
[20] J. Wright and W. Shyy, Int. J. Heat Mass Transf. **39**, 1183 (1996).
[21] L. Kleiser and U. Schumann, in *Proceedings of the 3rd GAMM Conference on Numerical Methods in Fluid Mechanics*, edited by E. H. Hirschel (Vieweg, Braunschweig, 1980), p. 165.
[22] L. S. Tuckerman, J. Comput. Phys. **80**, 403 (1989).
[23] P. Le Quere, Phys. Fluids A **2**, 503 (1990).
[24] B. R. Ruddick and J. S. Turner, Deep-Sea Res. **26**, 903 (1979).
[25] P. F. Linden, Geophys. Astrophys. Fluid Dyn. **13**, 3 (1979).
[26] Y.-G. Park, J. A. Whitehead, and A. Gnanadeskian, J. Fluid Mech. **279**, 279 (1994).
[27] N. J. Balmforth, S. G. L. Smith, and W. R. Young, J. Fluid Mech. **355**, 329 (1998).
[28] S. Chandrasekhar, *Hydrodynamic and Hydromagnetic Stability*

(Dover, New York, 1981).
[29] C. Canuto, M. Y. Hussaini, A. Quarteroni, and T. A. Zang, *Spectral Methods in Fluid Dynamics* (Springer-Verlag, New York, 1988).
[30] D. B. Haidvogel and T. A. Zang, J. Comput. Phys. **30**, 167 (1979).
[31] J. Werne, J. Comput. Phys. **120**, 260 (1995).
[32] S. Takao and U. Narusawa, Int. J. Heat Mass Transf. **23**, 1283 (1980).
[33] H. E. Huppert and J. S. Turner, J. Fluid Mech. **100**, 367 (1980).
[34] U. Narusawa and Y. Suzukawa, J. Fluid Mech. **113**, 387 (1981).
[35] S. G. Schladow, E. Thomas, and J. R. Koseff, J. Fluid Mech. **236**, 127 (1992).
[36] J. J. Rohr, E. C. Itsweire, and C. W. Van Atta, Geophys. Astrophys. Fluid Dyn. **29**, 221 (1984).
[37] J. Rohr and C. Van Atta, J. Geophys. Res. **32**, 5481 (1987).
[38] C. F. Chen and F. Chen, J. Fluid Mech. **352**, 161 (1997).
[39] R. B. Lambert and J. W. Demenkow, J. Fluid Mech. **54**, 627 (1971).
[40] S. Orszag, J. Comput. Phys. **37**, 70 (1980).
[41] P. Le Quere and T. A. De Roquefort, J. Comput. Phys. **57**, 210 (1985).
[42] S. A. Thorpe, J. Fluid Mech. **32**, 693 (1968).